Universitat Autònoma de Barcelona

Design and characterization of dense and porous Fe-based alloys for biomedical and environmental applications

Yuping Feng

Tesi Doctoral

Programa de Doctorat en Ciència de Materials

Jordi Sort Viñas (director i tutor)

Eva Pellicer Vilà (directora)

Jordina Fornell Beringues (directora)

Departament de Física

Facultat de Ciències

2017

3. Results: compilation of articles

Chapter 3: Results: compilation of articles

In this Chapter, the results derived from the Thesis are presented as a compilation of articles. An extended abstract is included before each publication. A thorough discussion of the results is provided in the articles themselves.

3.1 Novel Fe-Mn-Si-Pd alloys: insights on mechanical, magnetic, corrosion and biocompatibility performance

In this article, we report on the design, fabrication and characterization of two new Fe-Mn-Si-Pd alloys. Based on recent *in-vitro* and *in-vivo* experiments, Fe-Mn based alloys have established as promising materials for biomedical applications. Depending on the Mn content, these alloys can be either ferromagnetic or non-ferromagnetic. Addition of Pd and Si can improve the biodegradability rates and enhance the resulting mechanical properties. In spite of previous works on this topic, the evolution of the structure and physical/chemical properties (mechanical, magnetic, wettability, corrosion performance, etc.) in the presence of simulated body fluids (i.e., during the course of biodegradation) have been rather overlooked. The cytotoxic effects of ion release during immersion tests and the consequences of surface oxidation and biodegradation on cell adhesion and proliferation are additional aspects that need to be investigated in detail for the subsequent use of this type of materials.

The present study focuses on the synthesis and characterization of ferromagnetic Fe-10Mn6Si1Pd and shape memory, paramagnetic Fe-30Mn6Si1Pd alloys (weight composition). The mechanical, magnetic, corrosion resistance, wettability and biocompatibility properties of these new materials, before and during the course of immersion tests in Hanks's solution, are investigated. From the biological point of view, both cytotoxicity and cell proliferation are analyzed in detail. Our results reveal that while the Fe-10Mn6Si1Pd alloy is ferromagnetic, Fe-30Mn6Si1Pd remains non-ferromagnetic both in the as-cast state and after short- and long-term immersion tests in Hank's solution. Both alloys exhibit outstanding mechanical properties compared to other Fe-based materials (e.g., larger hardness and lower Young's modulus than austenitic steels). From a biological viewpoint, both Fe-10Mn6Si1Pd and Fe-30Mn6Si1Pd are initially biocompatible. The more hydrophilic character of the Fe-10Mn6Si1Pd alloy (as assessed by wettability tests) favors the initial cell adhesion. However, the formation of a cracked, loosely attached, oxide layer in this case, facilitates a pronounced ion

release, hence hampering cell proliferation on the surface of this alloy to some extent, as compared to Fe-30Mn6Si1Pd.

From the obtained results, both alloys emerge as potential candidate materials to be utilized in the biomedical field. While the Fe-10Mn6Si1Pd alloy could be used for magnetically (wirelessly)-actuated microrobots (e.g., for drug delivery), the Fe-30Mn6Si1Pd alloy could find his spot in the orthopedic field because its non-magnetic character would make it compatible with NMR and MRI analyses.

Novel Fe-Mn-Si-Pd alloys: insights on mechanical, magnetic, corrosion and biocompatibility performance

Yu Ping Feng,[a] Andreu Blanquer,[b] Jordina Fornell,[*a] Huiyan Zhang,[a] Pau Solsona,[a] Maria Dolors Baró,[a] Santiago Suriñach,[a] Elena Ibáñez,[b] Eva García-Lecina,[c] Xinquan Wei,[d] Ran Li,[d] Lleonard Barrios,[b] Eva Pellicer,[a] Carme Nogués[b] and Jordi Sort[a,e]

[a]*Departament de Física, Universitat Autònoma de Barcelona, E-08193 Bellaterra, Spain*

[b]*Departament de Biologia Cel·lular, Fisiologia i Immunologia, Universitat Autònoma de Barcelona, E-08193 Bellaterra, Spain*

[c]*Surfaces Division, IK4-CIDETEC, Parque Tecnológico de San Sebastián, E-20009 Donostia, Spain*

[d] *Key Laboratory of Aerospace Materials and Performance, School of Materials Science and Engineering, Beihang University, 100191 Beijing, China*

[e]*Institució Catalana de Recerca i Estudis Avançats (ICREA), Passeig Lluís Companys 23, E-08010 Barcelona, Spain*

**Corresponding author. E-mail address: jordina.fornell@uab.cat*

Journal of
Materials Chemistry B

PAPER

View Article Online
View Journal | View Issue

Cite this: J. Mater. Chem. B, 2016, 4, 6402

Novel Fe–Mn–Si–Pd alloys: insights into mechanical, magnetic, corrosion resistance and biocompatibility performances†

Yu Ping Feng,[a] Andreu Blanquer,[b] Jordina Fornell,*[a] Huiyan Zhang,[a] Pau Solsona,[a] Maria Dolors Baró,[a] Santiago Suriñach,[a] Elena Ibáñez,[b] Eva García-Lecina,[c] Xinquan Wei,[d] Ran Li,[d] Lleonard Barrios,[b] Eva Pellicer,[a] Carme Nogués[b] and Jordi Sort[ae]

Received 3rd August 2016,
Accepted 23rd August 2016

DOI: 10.1039/c6tb01951j

www.rsc.org/MaterialsB

Two new Fe-based alloys, Fe–10Mn6Si1Pd and Fe–30Mn6Si1Pd, have been fabricated by arc-melting followed by copper mold suction casting. The Fe–30Mn6Si1Pd alloy mainly consists of ε-martensite and γ-austenite Fe-rich phases whereas the Fe–10Mn6Si1Pd alloy primarily contains the α-Fe(Mn)-ferrite phase. Additionally, Pd-rich precipitates were detected in both alloys. Good mechanical response was observed by nanoindentation: hardness values around 5.6 GPa and 4.2 GPa and reduced Young's moduli of 125 GPa and 93 GPa were measured for the as-prepared Fe–10Mn6Si1Pd and Fe–30Mn6Si1Pd alloys, respectively. Both alloys are thus harder and exhibit lower Young's modulus than 316L stainless steel, which is one of the most common Fe-based reference materials used for biomedical applications. Compared with the ferromagnetic Fe–10Mn6Si1Pd alloy, the paramagnetic Fe–30Mn6Si1Pd alloy is more appropriate to be used as an implant since it would be compatible for nuclear magnetic resonance (NMR) and magnetic resonance imaging (MRI) analyses. Concerning biocompatibility, the more hydrophilic Fe–10Mn6Si1Pd alloy shows improved cell adhesion but its pronounced ion leaching has a negative effect on the proliferation of cells. The influence of immersion in a simulated body fluid on the composition, microstructure, mechanical and magnetic properties of both alloys is assessed, and the correlation between microstructure evolution and physical properties is discussed.

1. Introduction

Over the past few years, the interest in novel permanent and biodegradable metallic alloys has been continuously increasing. While Ti alloys have been established as ideal materials for permanent orthopaedic implants, Mg-based and Fe-based alloys are considered as potential candidates for temporary medical biodegradable implants, such as stents or bone replacements.[1–5] The main advantage of biodegradable implants, compared with permanent ones, is that a secondary surgery for implant removal can be avoided, improving the patient's comfort and reducing the cost of medical treatment. Mg and its alloys are free from toxic elements, and exhibit fast biodegradability and a Young's modulus closer to that of the human bone. However, the high degradation rates of Mg alloys may limit their use in certain applications where the implant needs to stay in the body for at least a specific period of time. Furthermore, the accompanying considerable amounts of hydrogen release could impede a good connectivity between osteocytes and the alloy. Also, for some applications, the strength and ductility of Mg-alloys are not good enough for supporting our body.[3,6]

Recently, because of the good preliminary results obtained in *in vitro* and *in vivo* experiments, attention is being paid to Fe-based alloys.[7,8] However, the degradation rate of most Fe-based alloys is still too low to meet the requirements of degradable stent applications.[3] In addition, some Fe-based alloys are ferromagnetic, thus precluding their use in specific applications where nuclear magnetic resonance (NMR) or magnetic resonance imaging (MRI) analysis is required to monitor the patient's recovery after surgery.

[a] Departament de Física, Universitat Autònoma de Barcelona, E-08193 Bellaterra, Spain. E-mail: jordina.fornell@uab.cat
[b] Departament de Biologia Cellular, Fisiologia i Immunologia, Universitat Autònoma de Barcelona, E-08193 Bellaterra, Spain
[c] Surfaces Division, IK4-CIDETEC, Parque Tecnológico de San Sebastián, E-20009 Donostia, Spain
[d] Key Laboratory of Aerospace Materials and Performance, School of Materials Science and Engineering, Beihang University, 100191 Beijing, China
[e] Institució Catalana de Recerca i Estudis Avançats (ICREA), Passeig Lluís Companys 23, E-08010 Barcelona, Spain

† Electronic supplementary information (ESI) available. See DOI: 10.1039/c6tb01951j

During the last few years, FeMn,[3,9–12] FeMnPd[3,9] and FeMnSi[13] alloys with enhanced degradation rates and mechanical properties similar to those of 316L stainless steel have been manufactured for stent materials. The addition of Mn within the solubility limit of Fe reduces the standard electrode potential of Fe to make it more susceptible to corrosion.[3,9–12] The addition of noble alloying elements, such as Pd, can generate small and homogeneously dispersed Pd-rich precipitates that act as cathodic sites to induce microgalvanic corrosion.[3] Previous studies have shown that silicon addition to the Fe–30Mn alloy increases its corrosion rate. This fact has been attributed to a larger γ-austenite content, which corrodes faster than ε-martensite, in the alloys containing silicon.[13] Moreover, the tensile strength increases significantly with the increase of Si content in the Fe–Mn–Si alloy.[13,14] Besides, some Fe–Mn–Si alloys have been studied for a long time[13,15] because of their shape memory behavior, which may also be of interest for some applications in the biomedical field (*e.g.*, stents).[13] With the appropiate transformation temperature and microstructure, these ternary alloys might be used as self-expandable stents taking advantage of the superelasticity effect, thus minimizing the risk of damaging the vascular tissue due to inflammatory reactions produced by the balloon expansion in conventional stenting procedures using non-superelastic materials.[16]

The goal of this work is to obtain suitable Fe-based alloys with improved properties to be used in biomedical applications. With this purpose, two different compositions have been designed. On the one hand, the addition of 1 wt% of Pd to the ternary Fe–30Mn–6Si is expected to increase its degradation rate because of the formation of small and homogeneously dispersed Pd-rich precipitates. On the other hand, the addition of 6 wt% of Si to the ternary Fe–10Mn–1Pd, besides increasing the strength of the alloy, is expected to aid the healing process and help the immune system, as silicon is an essential mineral in the human body.[13] So far only the binary and ternary alloys have been investigated and hence the idea of our work is to produce quaternary alloys that take advantage of all the aforementioned properties in a synergetic way. In the present manuscript, two newly developed Fe–10Mn6Si1Pd and Fe–30Mn6Si1Pd alloys have been fabricated by arc-melting and copper-mold suction casting and their properties (magnetic, mechanical, corrosion resistance, wettability and biocompatibility) have been characterized. The use of this synthetic approach allows obtaining homogenous Fe-based alloys with Pd-rich precipitates and competitive properties compared to the up-to-date reported Fe-based materials.

While the Fe–10Mn6Si1Pd alloy is ferromagnetic, Fe–30Mn6Si1Pd remains non-magnetic both in the as-cast state and after short- and long-term immersion tests in Hank's solution. The evolution of microstructure and mechanical properties during the course of immersion experiments has also been assessed. From the biological point of view, two different parameters have been analyzed: cytotoxicity, which allows determining whether the partial dissolution of the alloy produces a decrease in the cell number with time; and proliferation, which enables the determination of not only if the alloy causes cytotoxicity, but also if cells can divide and proliferate (increase of their number over time).

2. Materials and methods

2.1. Materials

Commercial Fe (97%), Si (99%), Mn (99%) and Pd (99.95%) were mechanically milled in a shaker mill device (SPEX 8000 M) at room temperature, with a nominal composition of Fe–10Mn6Si1Pd and Fe–30Mn6Si1Pd (wt%). The powders were milled under an Ar atmosphere in a ball-to-powder weight ratio of 1:1 for 15 h. All the operations prior to milling (weighing the powder and sealing the container) were done in a glove box under an Ar atmosphere (<0.2 O_2 ppm, <0.1 H_2O ppm) to avoid oxidation or any other atmospheric contamination. Subsequently, the powders were consolidated using a uniaxial cold press under a pressure of 100 MPa to obtain disks of approximately 5 mm in thickness. Then, the disks were melted in a mini arc-melting furnance (MAM1, Edmund Bühler Lab Tec) under an Ar atmosphere and suction-casted in a copper mold to produce cylindrical rods of 3 mm in diameter and a few centimeters in length. The same procedure was used to produce a control Pd-free alloy for corrosion experiments with a nominal compostion of Fe–30Mn–6Si.

The real compositions of the as-cast rods, as measured by energy dispersive X-ray spectroscopy (EDX), were Fe–9.97Mn–5.71Si1.19Pd and Fe–29.17Mn5.76Si1.26Pd (wt%).

2.2. Immersion tests

Prior to immersion tests, pieces of 3 mm in diameter and 1 mm thickness of the as-cast alloys were cold-embedded in epoxy resin and ground up to P4000 grit with SiC. The alloys were then immersed in 28 ml of Hank's balanced salt solution at 37 ± 1 °C for different times, up to 120 days. The volume of solution was selected so as to conform with the ASTM-G31-72 norm.[17] Hank's balanced salt solution (HBSS) is a widely used simulated physiological fluid to reproduce *in vivo* conditions.[13,18,19] After immersion, the samples were removed from Hank's solution, rinsed with alcohol, and dried in air. The microstructure, mechanical properties and magnetic behavior were subsequently assessed as a function of immersion time. Also, 3 ml of Hank's solution were pipetted off to measure the ion released concentration of Fe, Mn, Si and Pd by inductively coupled plasma optical emission spectroscopy (ICP-OES). In parallel, alloys were also immersed in 1 ml of Dulbecco's modified Eagle's medium (DMEM, Gibco) with 10% foetal bovine serum (FBS, Gibco) and incubated under standard conditions (37 °C and 5% CO_2) for different times, to measure the ion release by ICP-OES under exactly the same conditions as used for the cell cultures. In order to ensure the tests are reproducible, three replicates were prepared and analyzed for each sample.

2.3. Structural characterization

Scanning electron microscopy (SEM) using a Zeiss Merlin microscope equipped with an energy dispersive X-ray spectroscope (EDX) was used for morphological and compositional analyses. X-ray diffraction (XRD) was carried out using a Philips X'Pert diffractometer using Cu Kα radiation. The measurements were performed in the angular range 25–100° with a step size of 0.04°. Differential scanning calorimetry (DSC) (Perkin Elmer,

DSC 8000) was used to detect the austenite to martensite phase transformation in the alloy with 30 wt% of Mn.

2.4. Characterization of physical and mechanical properties

Nanoindentation measurements were carried out on the as-cast and immersed samples using a UMIS nanoindenter from Fischer-Cripps Laboratories, with a Berkovich pyramid-shaped diamond indenter. Prior to nanoindentation, the as-cast samples were polished to mirror-like appearance using in the final step 1 μm of diamond particle solution. The roughness of the as-cast samples was measured using a Leica DCM 3D system that combines confocal and interferometry technologies. The maximum applied load in nanoindentation tests was 500 mN. The results were averaged over more than 20 indents to obtain statistically reliable data. The Berkovich hardness (H) and reduced Young's moduli (E_r) were evaluated from the load–displacement curves at the beginning of the unloading segments, using the method of Oliver and Pharr.[20] Compression tests were carried out on cylinder-shaped samples with an aspect ratio (length : diameter) of 2 : 1 at a strain rate of 2×10^{-4} s^{-1} using the equipment from MTS (CMT5105, 100 kN). Hysteresis loops were collected using a vibrating sample magnetometer (VSM) from Oxford Instruments, with a maximum applied magnetic field of 12 kOe at room temperature.

2.5. Electrochemical potentiodynamic polarization measurements and wettability

The corrosion behavior of the as-cast alloys was evaluated by potentiodynamic polarization, which was carried out in a single compartment, double-walled cell with a typical three-electrode configuration (connected to an Autolab 302N potentiostat/galvanostat) at 37 ± 1 °C in Hank's solution, analogous to the configuration we previously used for Ti-based biomaterials.[21] A double junction Ag/AgCl with 3 M KCl inner solution and 1 M NaCl outer solution was used as the reference electrode, while a Pt sheet was used as the counter-electrode. Prior to the measurements, the specimens were immersed in the electrolyte for 1 h to obtain the open circuit potential (OCP). Three samples of each composition were measured to prove good reproducibility. The upper and lower potential limits were set to −300 mV and +1500 mV with respect to the OCP. The scan rate was 0.5 mV s^{-1}.

To assess the wettability, the contact angles were determined by means of the sessile drop technique, using a surface analyzer (CAM 200, Iberlaser). The liquid utilized for the measurements was 1 μl droplets of Hank's solution at room temperature.

2.6. Cytotoxicity tests and proliferation assays

Saos-2 human osteosarcoma cells (ATCC) were cultured in DMEM with 10% FBS under standard conditions. To assess the cytotoxicity, alloy disks were cleaned with absolute ethanol, introduced into a 4-multiwell culture plate and sterilized by UV light for at least 2 h. Once sterilized, 50 000 cells were seeded into each well and cultured for 1, 3, 7 and 40 days. Cell viability on disk surfaces was evaluated using the Live/Dead Viability/Cytotoxicity kit for mammalian cells (Invitrogen), according to the manufacturer's protocol. Images from different regions of the alloy disk and from the control culture (without disk) were captured using an Olympus IX71 inverted microscope equipped with epifluorescence. For proliferation assay, a total amount of 50 000 Saos-2 cells were seeded into each well of a 4-multiwell plate containing the alloy disk. After 24 h, disks with adhered cells on their surface were transferred to a 96-multiwell plate, and medium with 10% of Alamar Blue (Invitrogen) was added to each well and incubated for 4 h at 37 °C and 5% CO_2, with protection from direct light. Then, the supernatant was collected and the fluorescence was read using a Cary Eclipse fluorescence spectrophotometer (Agilent Technologies). Cells on the disk were incubated again with fresh medium, and the Alamar Blue analysis was repeated at 3, 7, 14 and 60 days. Negative controls without cells were also analyzed.

The same samples used for the cytotoxicity and cell proliferation assays were then processed to be observed by SEM. Cultured cells were rinsed twice in phosphate buffered saline (PBS), fixed in 4% paraformaldehyde (PFA, Sigma) in PBS for 45 min at room temperature and rinsed twice in PBS. Cell dehydration was performed in a series of ethanol solutions (50%, 70%, 90% and twice 100%), for 7 min each. Finally, samples were dried using hexamethyl disilazane (Electron Microscopy Sciences) for 15 min, mounted on special stubs and analyzed using a SEM.

2.7. Hemolysis test

To evaluate the hemocompatibility of the alloys, 1 cm^2 ml^{-1} Fe10MnSiPd and Fe30MnSiPd were soaked in 10 ml PBS in centrifuge tubes and kept at 37 °C for 30 min. Then, 0.2 ml of diluted blood (4 ml of human blood in 5 ml PBS) were added to the samples and kept at 37 °C for 1 h. Next, the tubes were centrifuged at 2500 rpm for 5 min. The supernatant from each tube was transferred to a well of a 24-well plate and the optical density (OD) was recorded using a spectrophotometer at 545 nm wavelength. The OD values of a negative control (10 ml PBS with 0.2 ml diluted blood) and a positive control (10 ml distilled water with 0.2 ml diluted blood) were also recorded. The hemolysis ratio (HR) was calculated according to the equation: HR = [(ODt − ODn)/(ODp − ODn)] × 100%. The ODt is the OD value of the tested group. The ODn and ODp are the OD values of negative and positive controls, respectively.

The blood was taken from the researcher responsible for the project. Following the advice of the Animal and Human Experimentation Ethics Committee of the Universitat Autònoma de Barcelona, this researcher gave her informed consent.

3. Results and discussion

3.1. Microstructure and compositional analyses

3.1.1. Morphology and crystallographic phase composition of the as-cast alloys. Fig. 1 shows the SEM micrographs (back-scattered electrons) of the Fe–10Mn6Si1Pd (panel a) and Fe–30Mn6Si1Pd (panel b) as-cast alloys. Both of them show the typical dendritic morphology: a lighter phase enriched in Fe (according to EDX analysis), embedded in a darker phase

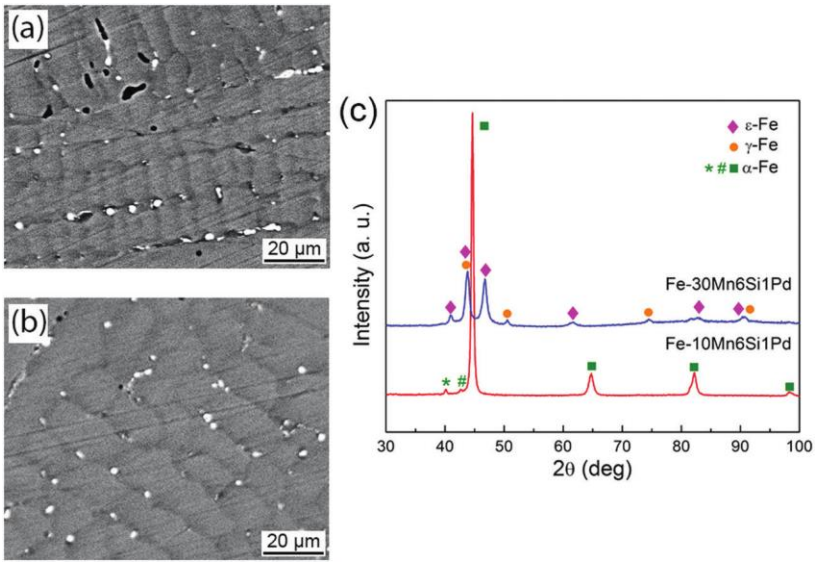

Fig. 1 SEM images of (a) Fe–10Mn6Si1Pd and (b) Fe–30Mn6Si1Pd polished alloys. (c) XRD patterns of as-cast Fe–10Mn6Si1Pd and Fe–30Mn6Si1Pd alloys. Note that the small peaks denoted with * and # belong to the α-Fe phase and come from the K_β and W L_α reflections, respectively. The other peaks come from K_α radiation.

slightly enriched in Si and Mn (see Fig. S1 in the ESI†). The bright spots distributed within the darker phase are Pd-rich precipitates (Fig. S1 in ESI†). The formation of noble Pd-rich precipitates is expected to induce microgalvanic corrosion, which is supposed to enhance the degradation rate of the alloys. The roughness averages (Ra) of the as-cast samples were 8.04 nm and 6.6 nm for the alloys with 10 and 30% of Mn, respectively. Fig. 1c illustrates the XRD patterns of as-cast Fe–10Mn6Si1Pd and Fe–30Mn6Si1Pd alloys. The alloy with 10 wt% Mn is composed of α-Fe (space group *Im*3*m* and cell parameter a = 2.88 Å). Conversely, the as-cast alloy with 30 wt% Mn mainly consists of ε-martensite ($P6_3/mmc$, a = 2.55 Å, c = 4.14 Å) and γ-austenite ($Fm3m$, a = 3.60 Å) phases.

The alloy with 30 wt% Mn is a shape memory alloy and can exhibit superelasticity or a shape memory effect depending on the stable phase at the test temperature. Both alloys were characterized in the as-cast state without subjecting them to any thermal treatment. Consequently, at room temperature, the alloy with 30% of Mn has a mixed microstructure (austenite and martensite phases), but by adjusting the testing temperature or subjecting the alloy to an appropriate heat treatment pure austenite, responsible for superelasticity behavior, or martensite, responsible for the shape memory effect, could be obtained. Differential scanning calorimetry (DSC) at 10 K min^{-1} was used to identify the transformation temperatures (Fig. S2 in ESI†). The final and initial temperatures of austenite, and the initial and final temperatures of martensite are, respectively: $A_f \approx 250$ °C, $A_s \approx 150$ °C, $M_s \approx 58$ °C and $M_f \approx -30$ °C. In agreement with DSC measurements and, as evidenced by XRD, the Fe–30Mn6Si1Pd alloy is a mixture of austenite and martensite at room temperature (Fig. 1). However, if the alloy was cooled to below M_s, (*i.e.*, $T < -30$ °C) and subsequently warmed up to room temperature in open air, the resulting phase would be only martensite and the alloy would exhibit shape memory behavior at room temperature.[22] In the same way, superelasticity would be expected above 250 °C.[23] Hence, this feature can broaden the application window of this particular alloy.

3.1.2. Surface morphology and chemical analyses as a function of immersion time. The morphological evolution of both alloys after immersion in Hank's solution for 1 and 4 months is illustrated in Fig. 2. After 1 month, two different regions can be distinguished on the surface of the Fe–10Mn6Si1Pd alloy:

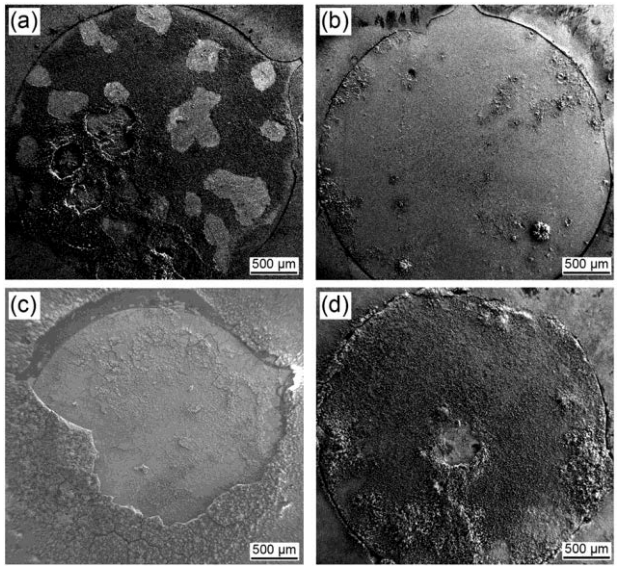

Fig. 2 Low magnification SEM micrographs of the: (a and c) Fe–10Mn6Si1Pd alloy after immersion in Hank's solution [for (a) 1 month and (c) 4 months] and (b and d) Fe–30Mn6Si1Pd alloy after immersion for (b) 1 month and (d) 4 months.

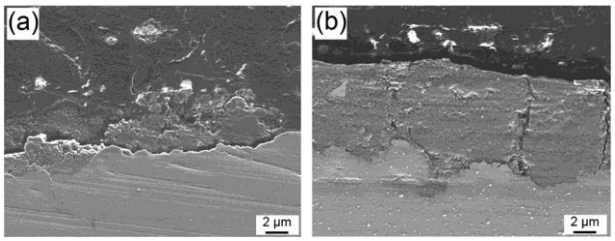

Fig. 3 Cross-section SEM images of (a) Fe–10Mn6Si1Pd and (b) Fe–30Mn6Si1Pd alloys after 1 month of immersion in Hank's solution.

a rougher region, covered with corrosion products, and a smoother region, free from corrosion products. The partial coverage with the rough layer indicates that this layer is probably not very well adhered to the surface of the alloy and tends to peel off upon cleaning the sample. Conversely, the alloy with 30% of Mn is completely covered with a well-adhered and considerably smoother oxide layer. Similar trends are observed after 4 months of immersion, *i.e.*, while a rather compact oxide layer covers the surface of the alloy with 30% Mn, a cracked and a peeled off oxide layer can be observed in the alloy with 10% of Mn. These observations reveal that the samples exhibit a characteristic "cracked-earth" appearance which is often encountered in these types of samples after immersion tests and probably caused by dehydration of the degradation layer after removal from the electrolyte.[19,24,25] Further evidence of poor and good adhesion of the oxide layer for the alloys with 10 and 30% of Mn, respectively, after immersion for one month in Hank's solution can be observed in the cross-section SEM images (Fig. 3). In the Fe–10Mn6Si1Pd alloy it was difficult to find a zone with the oxide layer completely attached to the surface, and the areas where the layer did not peel off were thin and often cracked. Conversely, in the Fe–30Mn6Si1Pd alloy, a compact 3–5 μm thick oxide layer was observed across the entire surface. EDX maps of both alloys after 1 month of immersion in Hank's solution revealed that the outermost layer covering the alloys had less amount of Fe and Mn than in the initially bulk material and it was enriched in O and P. Some Ca-rich agglomerates were also detected. Also, in both cases but, most clearly observed in the EDX mapping of the alloy with 30% of Mn, a Si-rich layer was formed next to the alloy, but note that the outermost layer is completely depleted of Si, indicating its fastest degradation.

After 4 months of immersion, the thickness of the oxide layer increased ($\sim$40 μm for the alloy with 30% Mn and $\sim$12 μm for the alloy with 10% Mn) but in the alloy with 10% of Mn it was still difficult to find a well-adhered corrosion product layer (Fig. S3 in the ESI†). The EDX maps shown in Fig. 4 reveal that the oxide layer formed in the Fe–30Mn6Si1Pd alloy is rich in Si and O and it is depleted of Fe and Mn, when compared with the elemental composition of the metallic material underneath. Si is known to be an element prone to oxidation. In fact, in alkaline solutions, the standard reduction potential (E^0) for the reaction $SiO_3^{2-} + 3H_2O + 4e^- \rightarrow Si + 6OH^-$ is -1.69 V. The standard potential for Pd, Fe and Mn are the following ones: $E^0_{Pd^{2+}/Pd} = 0.95$ V, $E^0_{Fe^{2+}/Fe} = -0.44$ V and $E^0_{Mn^{2+}/Mn} = -1.18$ V.[26] Therefore, among all these elements, silicon is the one with the more negative standard potential, thus probably more prone to be oxidized. Even though the kinetics of degradation/corrosion between Fe–30Mn6Si1Pd and Fe–10Mn6Si1Pd alloys are different, same trends were observed in terms of oxide/hydroxide formation as can be observed in the SEM cross-section image (Fig. S4 in the ESI†) of the alloy with 10% of Mn.

To gain further insight into the corrosion product layers, XRD analyses were carried out on the alloys after 1, 2 and 4 months of immersion in Hank's solution (Fig. S5 in the ESI†). The results are in fairly good agreement with SEM observations. No peaks were detected in the alloy with 10% of Mn as the corrosion product layers were thin and not continuous. Conversely, in the alloy with 30% of Mn additional peaks belonging to FeO and SiO_2 were observed after 2 and 4 months of immersion.

The amounts of Fe and Mn ions released from the Fe–10Mn6Si1Pd and Fe–30Mn6Si1Pd alloys after immersion in Hank's

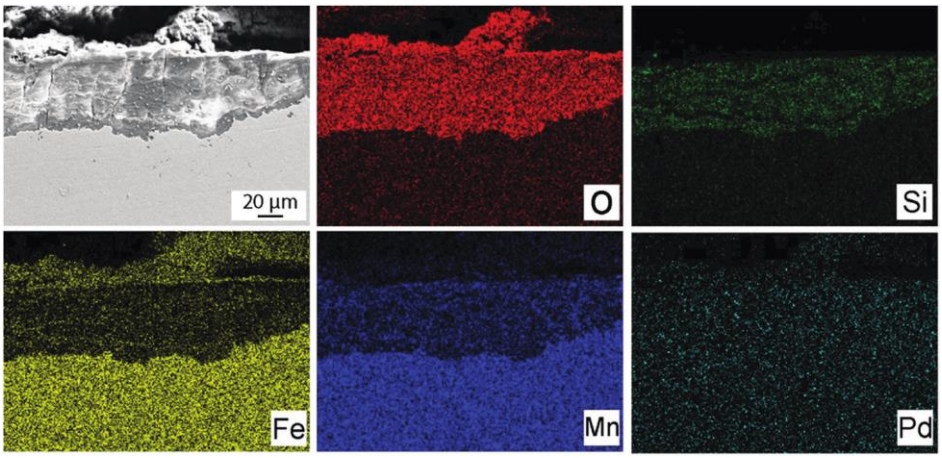

Fig. 4 Cross-section SEM images of Fe–30Mn6Si1Pd after immersion in Hank's solution for 4 months together with the element distributions of O, Si, Fe, Mn and Pd.

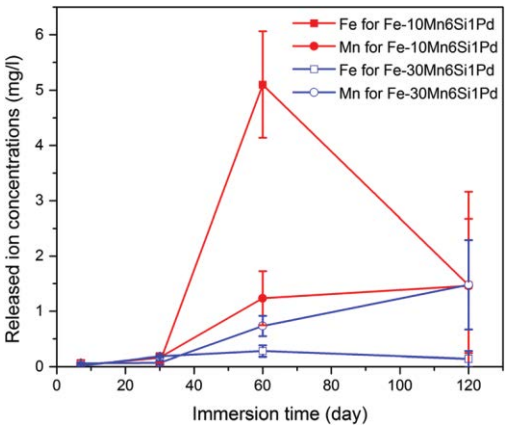

Fig. 5 ICP ion release concentrations of Fe–10Mn6Si1Pd and Fe–30Mn6Si1Pd alloys as a function of immersion time in Hank's solution, carried out in accordance with the ASTM-G31-72 norm, *i.e.*, using a large volume of Hank's solution (see text for details).

solution (28 ml) for 7, 30, 60 and 120 days are shown in Fig. 5. Larger amounts of the two main elements, Fe and Mn, are released from the alloy with 10 wt% of Mn even if the initial amount of Mn was lower in this case than for the alloy with 30% Mn. Therefore, the extraction tests, carried out in accordance with the ASTM-G31-72 standard, clearly reveal a higher degradation rate for this alloy. The Pd concentration was close to the detection limit of the equipment. As a general trend, a sharp increase of ion concentration with immersion time is observed; however, after 60 days, the increase of ion concentrations tends to level off. The parabolic shape of the ion concentration curves has been previously attributed to the formation of degradation products on the alloy surface. This oxide/hydroxide degradation layer hinders the ion release as the alloy is not in direct contact with media and degradation needs to take place by diffusion of Fe and Mn ions through the layer.[19,25] These results are in good agreement with our SEM observations where thicker and denser degradation layers are observed for the alloy with 30% of Mn and thinner and looser ones are formed in the alloy with 10% of Mn. In addition, a drastic reduction in the Fe ion concentration is observed after long-term immersion of the Fe–10Mn6Si1Pd alloy. This was accompanied by the formation of particle precipitates at the bottom of the Hank's solution container, probably in the form of Fe oxides or hydroxides, which were excluded for the ion release analyses. The differences observed between both alloys (*i.e.* ion release and hydro(oxide) formation) can be mainly attributed to the different microstructures of the alloys. While in the Fe–10Mn6Si1Pd alloy atoms are arranged in a single crystal structure (the body-centered cubic crystal structure of Fe with Mn atoms occupying substitutional positions), in the Fe–30Mn6Si1Pd alloy two crystal structures (a face-centered cubic and a hexagonal structure) coexist. Hence, different corrosion/degradation characteristics are expected between both alloys.

3.2. Evolution of magnetic and mechanical properties

The magnetic behavior of both alloys before and after immersion is compared in Fig. 6. In the as-cast state the alloy with 10% Mn is ferromagnetic, as it is mainly composed of the ferrite phase. In contrast, the alloy with 30% Mn is mainly paramagnetic as a result of the non-magnetic nature of the γ-austenite and ε-martensite phases.

After immersion, the magnetization of the ferromagnetic Fe–10Mn6Si1Pd alloy remains almost unaltered, while the coercivity decreases slightly. Conversely, the Fe–30Mn6Si1Pd alloy does not become ferromagnetic after immersion in Hank's solution. In view of these magnetic properties, these two alloys could find different applications in the biomedical field. While the Fe–10Mn6Si1Pd alloy could be used as a building block in magnetically (wirelessly)-actuated microrobots (*e.g.*, for drug delivery),[27,28] the Fe–30Mn6Si1Pd alloy would be more appropriate to be used as an orthopaedic implant because its non-magnetic character would make it compatible for NMR and MRI analyses.

The mechanical properties of the as-cast and immersed alloys were measured by nanoindentation. Compression tests were also performed on the as-cast materials. Note that the purpose of carrying out nanoindentation in the alloys after immersion was to capture the mechanical properties of the

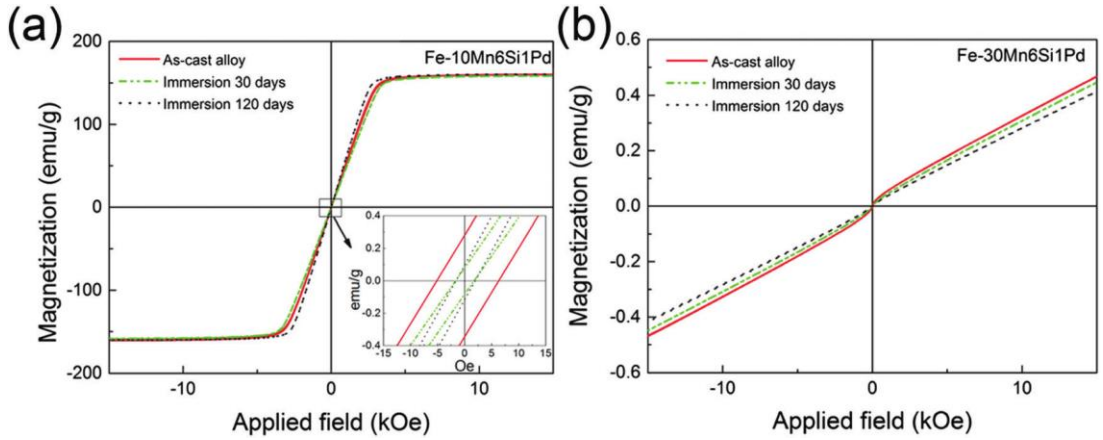

Fig. 6 Dependence of the magnetization as a function of applied magnetic field for Fe–10Mn6SiPd and Fe–30Mn6SiPd as a function of immersion time. The inset in (a) in an enlargement of the central part of the hysteresis loop.

corrosion layers formed in the course of immersion tests rather than to study the overall mechanical behavior of the alloys.

Fig. S6 (ESI†) shows the typical load–unload curves of the Fe–10Mn6Si1Pd and Fe–30Mn6Si1Pd alloys after 1-month immersion. For this particular case, the maximum penetration depth is 2.2 μm for the alloy with 10% Mn and 2.8 μm for the alloy with 30% Mn. The measurements carried out after 1 month of immersion show that the penetration depth is larger than the thickness limit that is usually considered as necessary in order to avoid the contribution from the substrate or the underlying material in the obtained results (typically, the maximum penetration depth must be lower than 1/10th the thickness of the sample[20]). Hence, especially for short-term immersion, H and E_r of the oxide layers are influenced by the properties of the bulk material. For longer immersion times, the oxide layers become thicker and the obtained values of H and E_r are thus mainly those of these oxide layers.

The dependencies of E_r and H for both samples as a function of immersion time are presented in Fig. 7. Both in the as-cast state and after immersion, the Fe–10Mn6Si1Pd alloy exhibits larger hardness than the Fe–30Mn6Si1Pd alloy. Since Mn is mechanically harder than Fe, different H values in the as-cast state are probably due to the dissimilar crystallographic phases that constitute these alloys. Namely, the presence of austenite (mechanically softer phase) probably contributes to the observed lower hardness in the Fe–30Mn6Si1Pd alloy.

Compression tests performed on the as-cast alloys (see Fig. S7 in the ESI†) shed further light on the mechanical behavior of these quaternary alloys. The stress–strain curves reveal that these alloys exhibit work-hardening behavior, which is particularly noticeable for the Fe–30Mn6Si1Pd material. Such work hardening has been reported in the literature in the binary Fe–30Mn alloy,[29,30] Fe–Mn–Si[13] or Fe–Mn–C,[30] and is generally ascribed to a deformation-induced martensitic transformation and/or accumulation of dislocations and mechanical twinning. Under the action of mechanical stress, austenite tends to transform into martensite, resulting in pronounced plasticity (larger than 40% for Fe–30Mn6Si1Pd). The Young's moduli determined from compression tests are 50.3 GPa for Fe–10Mn6Si1Pd and 59.7 GPa for Fe–30Mn6Si1Pd. The yield stress values are approximately 650 MPa and 270 MPa, respectively. These values are in good agreement with those of similar alloys reported in the literature.[13,30,31] It should be noted that the Young's moduli obtained from nanoindentation are larger than those from compression tests. Similarly, the yield stress (σ_y) that would be determined from nanoindentation using a constraint factor equal to 3 (*i.e.*, $H = 3\sigma_y$) is much larger than the σ_y values from compression tests. These effects can be understood as a direct consequence of the work hardening behavior. Namely, while E and σ_y from compression tests are obtained in the purely elastic regime (*i.e.*, before work hardening has occurred), the values of E_r and H from nanoindentation are obtained after both, plastic and elastic, deformations have occurred. In other words, the values of H and E_r from nanoindentation are already influenced by the work-hardening that occurs in the investigated alloys during the course of nanoindentation tests.

As shown in Fig. 7, in both alloys, H and E_r progressively decrease with the immersion time. The formation of surface oxides cannot explain this result by itself, since usually oxide materials are mechanically harder and exhibit higher Young's modulus than metallic alloys. However, as already discussed, these oxide layers are not flat and smooth. Actually, they tend to show a particulate and porous surface appearance (see inset in Fig. 7a). The occurrence of surface roughness and porosity is known to reduce both H and E_r.[4] Remarkably, E_r of both alloys reaches values close to 20 GPa after long-term immersion, a value which is close to the Young's modulus of human bones (3–27 GPa), hence favoring good biomechanical compatibility between an eventual implant and the neighboring bone tissue.[32] The dissimilar surface porosity between the two investigated alloys can also contribute to the different values of hardness after long-term immersion, besides the aforementioned role of the crystallographic phases constituting the two systems.

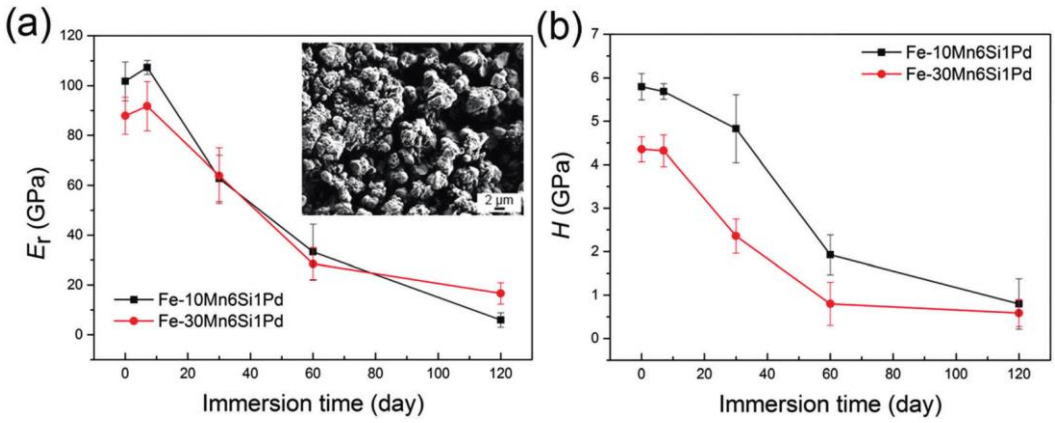

Fig. 7 Dependence of (a) reduced Young's modulus (E_r) and (b) hardness (H) for Fe–10Mn6Si1Pd and Fe–30Mn6Si1Pd as a function of immersion time. The inset in (a) shows an on-top high-resolution SEM image of the corrosion oxide layer corresponding to the Fe–30Mn6Si1Pd alloy after immersion for 120 days, where it can be seen that it shows a rather particulate and porous morphology.

3.3. Corrosion behavior

The potentiodynamic polarization curves obtained for the Fe–10Mn6Si1Pd and Fe–30Mn6Si1Pd alloys in Hank's solution are illustrated in Fig. 8. For comparison purposes, the potentiodynamic polarization curve of Fe–30Mn–6Si is also provided. The three alloys showed a similar profile; namely, they underwent rapid corrosion immediately after the E_{corr} values were surpassed pointing to a uniform corrosion mechanism, probably related to metal dissolution. At approximately 0.5 V *vs.* Ag/AgCl j_{corr} stabilized. This passive region could be ascribed to the protective/blocking effect impaired by the oxide layers formed on the alloy. E_{corr} for the Fe–10Mn6Si1Pd alloy is shifted towards more positive values compared to the quaternary alloy with 30 wt% Mn, reflecting the different chemical composition of the material and suggesting a delayed onset of material corrosion.

The potentiodynamic curve of the control ternary alloy exhibits a corrosion potential (E_{corr}) of 0.70 V. This value is slightly more positive than that of the quaternary alloy with 10% of Mn (E_{corr} = 0.63 V) but lower than that of the quaternary alloy with 30% of Mn (E_{corr} = 0.77 V). Therefore, it seems that the addition of 1% of Pd to the ternary Fe–30Mn6Si alloy triggers the onset of corrosion. It is difficult to draw meaningful conclusions regarding the corrosion rate based on the electrochemical polarization curves. Nevertheless, Liu *et al.*[13] demonstrated that the Fe–30Mn6Si alloy exhibits a higher corrosion rate than both Fe30Mn and pure iron. Previous ICP results (Fig. 5) indicate that for short immersion times (7 and 30 days) the total amount of ions released is slightly larger for the alloy with 30% Mn. After long-term immersion, though, the alloy with 10% Mn degrades considerably more than the alloy with 30% Mn. This suggests that the oxide layer formed on the Fe–30Mn6Si1Pd alloy is more compact, which further hinders ion release to some extent and slows down biodegradation. Indeed, cross-section SEM analyses (Fig. 4) indicate that the oxide layer for the Fe–10Mn6Si1Pd alloy is much thinner and discontinuous. Even though both potentiodynamic polarization curves are very similar, the lower corrosion potential and the less pronounced slope of the initial part of the anodic branch for the quaternary alloy with 30% of Mn might explain the different behavior observed between both alloys during the degradation experiments; however, for longer immersion periods similar degradation/corrosion behavior is expected for both quaternary compositions.

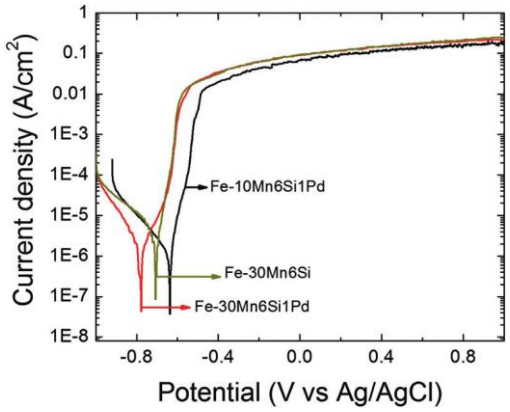

Fig. 8 Potentiodynamic polarization curves corresponding to the two quaternary Fe-based alloys, as well as the ternary Fe–30Mn6Si alloy (for the sake of comparison), in Hank's solution at 37 °C.

3.4. Wettability

Contact angle measurements assessed in Hank's solution medium are presented in Fig. 9. The alloy with 30% Mn exhibits a sligthly higher contact angle (82 ± 4°) than the alloy with 10% Mn (67 ± 6°). Typically, the contact angle value can be regarded as a parameter indicative of adhesion properties: smaller contact angles indicate better adhesion properties. Materials that exhibit contact angles larger than 90° are hydrophobic and are expected to exhibit poorer cell adhesion.[33] Consequently, the lower wetting angle measured in the Fe–10Mn6Si1Pd alloy compared to that observed in the Fe–30Mn6Si1Pd alloy may be indicative of improved cell adhesion for this alloy in the as-cast state.

3.5. Biocompatibility

Concerning the biocompatibility of alloys, two different types of analyses were performed: cytotoxicity and cell proliferation. Cytotoxicity analysis allows determining whether the alloy produces a cytotoxic effect (*i.e.*, a decrease in the live cell number with time), whereas cell proliferation analysis allows assessing whether cells growing on the alloy can proliferate (*i.e.*, increase their number over time).

A Live/Dead Viability/Cytotoxicity kit was used to determine the cytotoxicity at different time intervals for each composition. As shown in Fig. 10(a–f), after cell culturing for 1 day, the number of Saos-2 cells attached to the surface of Fe–10Mn6Si1Pd was higher than for Fe–30Mn6Si1Pd. This result is in agreement with the lower contact angle measured for the Fe–10Mn6Si1Pd alloy (Fig. 9), which favors cell adhesion. Indeed, previous studies have reported that 64° contact angles allowed an optimal cell adhesion compared with 90° contact angles, considered as hydrophobic surfaces.[34] The number of live cells after one day in culture was higher than 90% in both cases. However, after 3 and 7 days of culture, the results were reversed: the number of live cells on Fe–10Mn6Si1Pd was dramatically reduced, whereas it increased for cells cultured on the Fe–30Mn6Si1Pd alloy. Finally, after 40 days of culture very few cells remained attached to the surface of the Fe–10Mn6Si1Pd alloy, but the surface of Fe–30Mn6Si1Pd was still covered with a monolayer of live Saos-2 cells.

The results of Saos-2 cell proliferation can be seen in Fig. 10g. After one day of culture, the fluorescence intensity of live cells on the Fe–10Mn6Si1Pd alloy was more than three

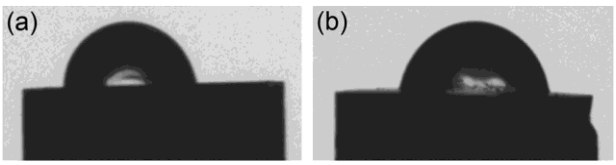

Fig. 9 Contact angle measurements for (a) Fe–10Mn6Si1Pd and (b) Fe–30Mn6Si1Pd, both assessed in Hank's solution medium.

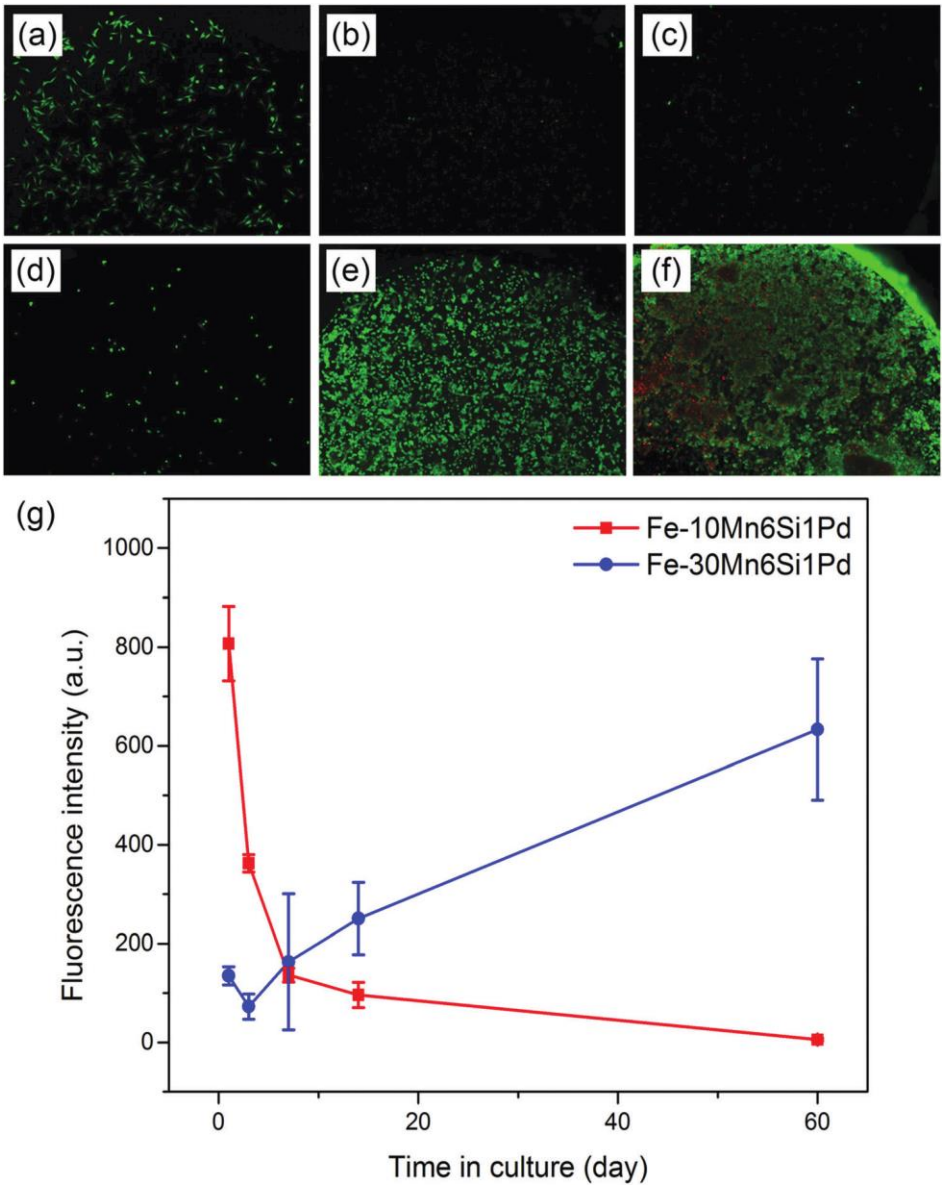

Fig. 10 Saos-2 cells cultured on Fe–10MnSiPd and Fe–30MnSiPd alloys. Cell viability on (a–c) Fe–10MnSiPd and (d–f) Fe–30MnSiPd alloys at: (a and d) 1 day, (b and e) 7 days and (c–f) 40 days. Live cells stained green and dead cells stained red. (g) Saos-2 cell proliferation on both alloy surfaces measured by Alamar Blue fluorescence at 1, 3, 7, 14 and 60 days.

times the value of cells on the Fe–30Mn6Si1Pd alloy. However, the total cell number on the Fe–10Mn6Si1Pd alloy decreased with time, becoming almost null after 60 days, while for the Fe–30Mn6Si1Pd alloy it progressively increased with culture time.

One possible explanation for the observed trend in cell viability and proliferation on the two alloys could be the pronounced degradation of the Fe–10Mn6Si1Pd alloy that occurs upon immersion. However, the ICP analyses carried out following the ASTM-G31-72 norm (Fig. 5) did not evidence pronounced ion release during the first 30 days of immersion. Probably, the large volume of Hank's solution used precludes a clear detection, by ICP, of the alloys' dissolution during the first days of immersion, in spite of the obvious formation of a corrosion oxide layer after a few weeks inside the Hank's solution (Fig. 2 and 3). To better understand the cytotoxicity of the two alloys, ICP analyses were also carried out on droplets extracted from the small volumes of DMEM with 10% FBS required for the cell culture assays. Fig. 11 reveals that under such concentrated conditions, pronounced ion release takes place from the very few days of immersion and, as expected, the Fe–10Mn6Si1Pd alloy degrades much faster than the Fe–30Mn6Si1Pd one, in agreement with Fig. 5. The pronounced ion release, together with the poor adhesion of the corrosion oxide layer in the Fe–10Mn6Si1Pd alloy (Fig. 2 and 3), probably accounts for the progressive decrease of live cells in this particular material.

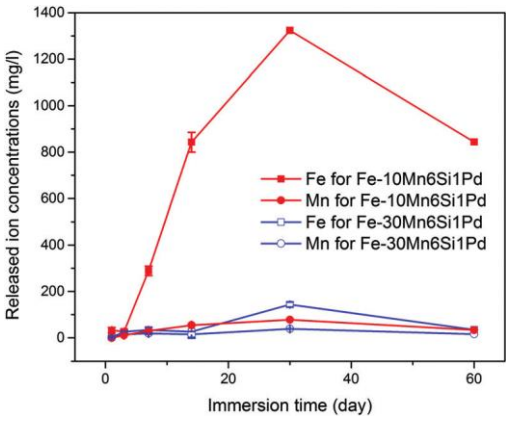

Fig. 11 Evolution of the ICP ion release concentrations of Fe–10Mn6Si1Pd and Fe–30Mn6Si1Pd alloys as a function of immersion time in Hank's solution under the same conditions used in the biological tests, *i.e.* with a small volume of solution (see the text for details).

Regarding cell morphology, SEM analysis of Saos-2 cells grown on alloy surfaces showed differences in shape and spreading between compositions and time intervals (Fig. 12). After 24 h of culture, cells observed on top of the Fe–10Mn6Si1Pd alloy presented a flattened and polygonal morphology with membrane projections. However, after 3 days of culture, a decrease in the number of cells was observed, and those still remaining on the alloy no longer completely adhered to the surface. They were round in shape, a sign of the difficulty for the cells to remain attached. Conversely, although a relatively small amount of cells were attached to the surface of the Fe–30Mn6Si1Pd alloy after 1 day, some of them were well adhered, with fusiform and flattened shapes. In this case, the number of well-spread cells increased with time, achieving a monolayer of cells after long-term culture.

Altogether, the results indicate a completely different behavior of the cells on top of both alloys. Cells initially adhered more easily onto the Fe–10Mn6Si1Pd alloy than on the Fe–30Mn6Si1Pd one, as expected by the higher hydrophilicity of the Fe–10Mn6Si1Pd surface.[34] But, eventually, the ions and debris released into the medium due to the degradation of the Fe–10Mn6Si1Pd alloy produced a negative effect on the cells, resulting in their detachment and subsequently death. Contrarily, the few cells that were able to attach to the Fe–30Mn6Si1Pd alloy surface were able to remain adhered over time and proliferate. This is in accordance with the SEM images of the 30% Mn alloy after 1 month of immersion in Hank's solution, which showed that the surface of the alloy was completely covered with a well-adhered and considerably smooth oxide layer which, in turn, hinders ion release and degradation. In contrast, the alloy with 10% Mn exhibited a cracked and loose oxide layer, which facilitates ion release, hence hampering cell proliferation on the alloy surface. Indirect studies performed with the Fe–10Mn6Si1Pd alloy showed that cytotoxicity was not increased in cells growing in the presence of this alloy but not in direct contact with it (see Fig. S8 in the ESI†). This confirms that the material is not cytotoxic by itself but the cracking and oxide formation on the surface hinders cell adhesion. Adhesion is mandatory for all adherent cells, as is the case of Saos-2 cell; when cells cannot adhere, they die.

3.6. Hemolysis

The HRs of Fe–10Mn6Si1Pd and Fe–30Mn6Si1Pd were 1.6 and 0.7, respectively. Both values were lower than 5%, indicating that both alloys are non-hemolytic, according to the Standard Practice for Assessment of Hemolytic Properties of Materials (ASTM-F756-08). Thus, both alloys could be good candidates for bioimplant devices.

4. Conclusions

1. Structural analyses reveal that the Fe–30Mn6Si1Pd alloy consists of ε-martensite, γ-austenite and homogeneously dispersed Pd-rich precipitates, while the Fe–10Mn6Si1Pd alloy contains α-ferrite and Pd-rich precipitates. In the as-cast state, good mechanical response was observed by nanoindentation: hardness values of 5.6 GPa and 4.2 GPa and reduced Young's moduli of 125.2 GPa and 93.1 GPa were measured for the Fe–10Mn6Si1Pd and Fe–30Mn6Si1Pd alloys, respectively, by nanoindentation. Work hardening behavior was observed

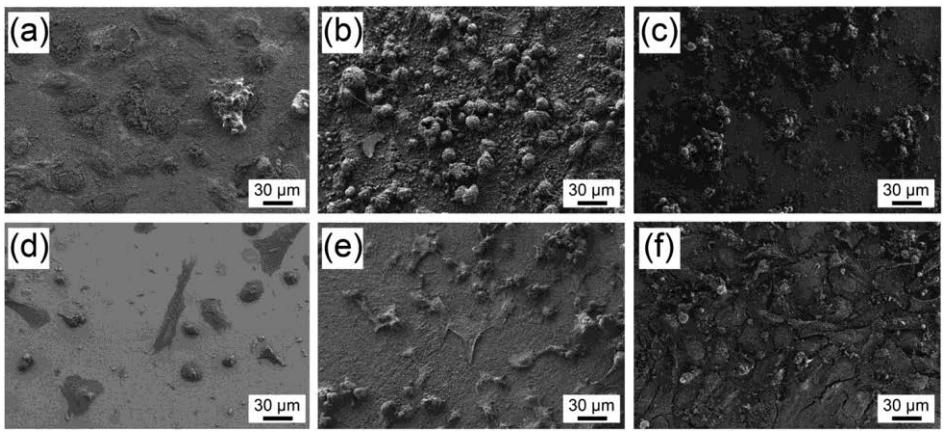

Fig. 12 SEM images of Saos-2 cells grown on (a–c) Fe–10MnSiPd and (d–f) Fe–30MnSiPd after (a and d) 1 day, (b and e) 3 days and (c and f) 7 days.

during compression tests, with total strain values exceeding 30% in both alloys.

2. Contrary to the ferromagnetic response of the Fe–10Mn6Si1Pd alloy, the paramagnetic Fe–30Mn6Si1Pd alloy is more appropriate to be used as an implant since it would be compatible for nuclear magnetic resonance and magnetic imaging analyses.

3. A loose oxide layer tends to form with immersion time in the Fe–10Mn6Si1Pd alloy, whereas the corrosion layer is more robust for the Fe–30Mn6Si1Pd alloy. As a consequence, a higher ion release concentration is observed for the alloy with 10% Mn.

4. The formation of rough and porous oxide layers on the surface of the alloys during immersion contributes to the decrease of the indentation hardness and reduced Young's modulus with immersion time, while virtually no variations in the overall magnetic properties of both samples are observed.

5. Both Fe–10Mn6Si1Pd and Fe–30Mn6Si1Pd are initially biocompatible. The more hydrophilic character of the Fe–10Mn6Si1Pd alloy (as assessed by wettability tests) favors the initial cell adhesion. However, the formation of a cracked, loosely attached, oxide layer in this case, facilitates pronounced ion release, hence hampering cell proliferation on the surface of this alloy, as compared to Fe–30Mn6Si1Pd.

6. Overall, the Fe–30Mn6Si1Pd alloy is a promising candidate for biodegradable implant applications since it combines the non-magnetic character with good Saos-2 cell proliferation.

Acknowledgements

This work was partially funded by the 2014-SGR-1015 project from the Generalitat de Catalunya and the MAT2014-57960-C3-1-R (co-financed by the *Fondo Europeo de Desarrollo Regional*, FEDER), the MAT2014-57960-C3-2-R and MAT2014-57960-C3-3-R projects from the Spanish *Ministerio de Economía y Competitividad* (MINECO). Dr Eva Pellicer is grateful to MINECO for the "Ramon y Cajal" contract (RYC-2012-10839).

References

1 Y. H. Yun, Z. Y. Dong, N. Lee, Y. J. Liu, D. C. Xue, X. F. Guo, J. Kuhlmann, A. Doepke, H. B. Halsall, W. Heineman, S. Sundaramurthy, M. J. Schulz, Z. Z. Yin, V. Shanov, D. Hurd, P. Nagy, W. F. Li and C. Fox, *Mater. Today*, 2009, **12**, 22.
2 B. Zberg, P. J. Uggowitzer and J. F. Loffler, *Nat. Mater.*, 2009, **8**, 887.
3 M. Schinhammer, A. C. Hanzi, J. F. Loffler and P. J. Uggowitzer, *Acta Biomater.*, 2010, **6**, 1705.
4 E. Pellicer, S. Gonzalez, A. Blanquer, S. Surinach, M. D. Baro, L. Barrios, E. Ibanez, C. Nogues and J. Sort, *J. Biomed. Mater. Res., Part A*, 2013, **101**, 502.
5 Y. Ding, Y. Li, J. Lin and C. Wen, *J. Mater. Chem. B*, 2015, **3**, 3741.
6 J. Kubasek, D. Vojtech, J. Lipov and T. Ruml, *Mater. Sci. Eng., C*, 2013, **33**, 2421.
7 M. Peuster, C. Hesse, T. Schloo, C. Fink, P. Beerbaum and C. von Schnakenburg, *Biomaterials*, 2006, **27**, 4955.
8 R. Waksman, R. Pakala, R. Baffour, R. Seabron, D. Hellinga and F. O. Tio, *J. Interv. Cardiol.*, 2008, **21**, 15.
9 F. Moszner, A. S. Sologubenko, M. Schinhammer, C. Lerchbacher, A. C. Hanzi, H. Leitner, P. J. Uggowitzer and J. F. Loffler, *Acta Mater.*, 2011, **59**, 981.
10 M. Schinhammer, C. M. Pecnik, F. Rechberger, A. C. Hanzi, J. F. Loffler and P. J. Uggowitzer, *Acta Mater.*, 2012, **60**, 2746.
11 H. Hermawan, H. Alamdari, D. Mantovani and D. Dube, *Powder Metall.*, 2008, **51**, 38–45.
12 H. Hermawan, D. Dube and D. Mantovani, *J. Biomed. Mater. Res., Part A*, 2010, **93**, 1.
13 B. Liu, Y. F. Zheng and L. Q. Ruan, *Mater. Lett.*, 2011, **65**, 540.
14 Z. G. Xu, M. A. Hodgson and P. Cao, *Mater. Sci. Eng., A*, 2015, **630**, 116.
15 S. N. Balo, *J. Supercond. Novel Magn.*, 2013, **26**, 1085.
16 L. Petrini and F. Migilavacca, *J. Metall.*, 2011, **2011**, 501483.
17 ASTM Standard G31-72, Standard Practice for Laboratory Immersion Corrosion Testing of Metals, ASTM Standards, Philadelphia, PA, USA, 2004.
18 H. Hermawan, A. Purnama, D. Dube, J. Couet and D. Mantovani, *Acta Biomater.*, 2010, **6**, 1852.
19 M. Moravej, A. Purnama, M. Fiset, J. Couet and D. Mantovani, *Acta Biomater.*, 2010, **6**, 1843.
20 W. C. Oliver and G. M. Pharr, *J. Mater. Res.*, 1992, **7**, 1564.
21 J. Fornell, E. Pellicer, N. Van Steenberge, S. Gonzalez, A. Gebert, S. Surinach, M. D. Baro and J. Sort, *Mater. Sci. Eng., A*, 2013, **559**, 159.
22 B. H. Jiang, T. Tadaki, H. Mori and T. Y. Hsu, *Mater. Trans., JIM*, 1997, **38**, 1072.
23 I. P. Spiridon, N. M. Lohan, M. G. Suru, E. Mihalache, L. G. Bujoreanu and B. Pricop, *Met. Sci. Heat Treat.*, 2016, **57**, 548.
24 M. Schinhammer, P. Steiger, F. Moszner, J. F. Loffler and P. J. Uggowitzer, *Mater. Sci. Eng., C*, 2013, **33**, 1882.
25 M. Schinhammer, I. Gerber, A. C. Hanzi and P. J. Uggowitzer, *Mater. Sci. Eng., C*, 2013, **33**, 782.
26 W. M. Haynes, *Handbook of Chemistry and Physics*, CRC Press, 94th edn, 2013.
27 S. Schuerle, S. Pane, E. Pellicer, J. Sort, M. D. Baro and B. J. Nelson, *Small*, 2012, **8**, 1498.
28 M. A. Zeeshan, S. Pane, S. K. Youn, E. Pellicer, S. Schuerle, J. Sort, S. Fusco, A. M. Lindo, H. G. Park and B. J. Nelson, *Adv. Funct. Mater.*, 2013, **23**, 823.
29 X. Liang, J. R. McDermid, O. Bouaziz, X. Wang, J. D. Embury and H. S. Zurob, *Acta Mater.*, 2009, **57**, 3978.
30 X. Wang, H. S. Zurob, J. D. Embury, X. Ren and I. Yakubtsov, *Mater. Sci. Eng., A*, 2010, **527**, 3785.
31 A. Francis, Y. Yang, S. Virtanen and A. R. Boccaccini, *J. Mater. Sci.: Mater. Med.*, 2015, **26**, 138.
32 X. N. Gu, Y. F. Zheng, S. P. Zhong, T. F. Xi, J. Q. Wang and W. H. Wang, *Biomaterials*, 2010, **31**, 1093.
33 J. H. Wei, T. Igarashi, N. Okumori, T. Igarashi, T. Maetani, B. L. Liu and M. Yoshinari, *Biomed. Mater.*, 2009, **4**, 045002.
34 D. P. Dowling, I. S. Miller, M. Ardhaoui and W. M. Gallagher, *J. Biomater. Appl.*, 2011, **26**, 327.

Supporting Information

Novel Fe-Mn-Si-Pd alloys: insights on mechanical, magnetic, corrosion and biocompatibility performance

Yu Ping Feng,[a] Andreu Blanquer,[b] Jordina Fornell,[*a] Huiyan Zhang,[a] Pau Solsona,[a] Maria Dolors Baró,[a] Santiago Suriñach,[a] Elena Ibáñez,[b] Eva García-Lecina,[c] Xinquan Wei,[d] Ran Li,[d] Lleonard Barrios,[b] Eva Pellicer,[a] Carme Nogués[b] and Jordi Sort[a,e]

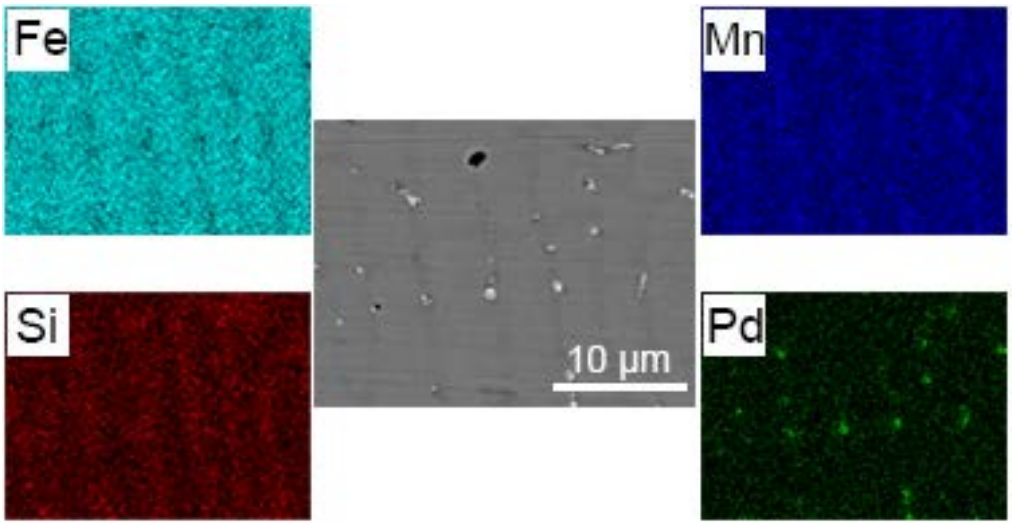

Fig. 1S: EDX elemental mapping of the Fe-30Mn6Si1Pd alloy. Mainly 3 regions are distinguished: light grey dendrites (enriched in Fe), darker regions slightly enriched in Si and Mn and small Pd-rich precipitates randomly distributed within the darker grey areas.

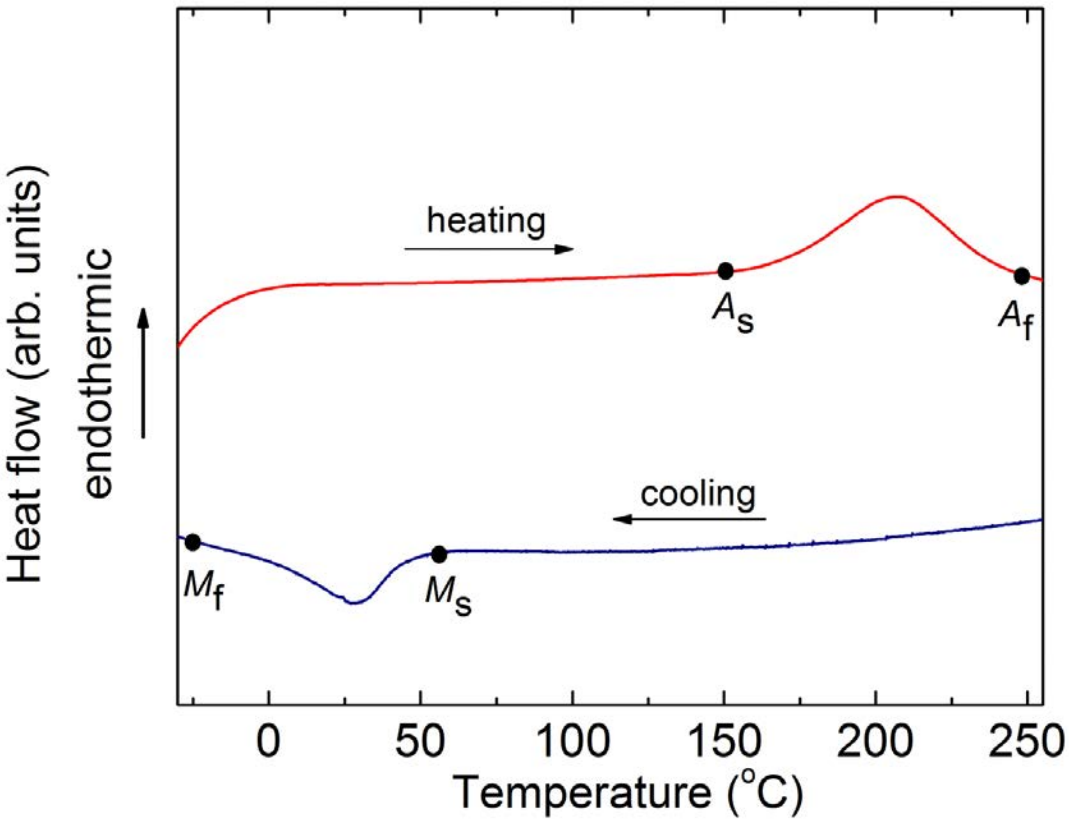

Fig. 2S: DSC curves of the Fe-30Mn6Si1Pd alloy. The austenite finish and start temperatures, and the martensite start and finish temperatures are $A_f \approx 250$ °C, $A_s \approx 150$ °C, $M_s \approx 58$ °C and $M_f \approx -30$ °C, respectively.

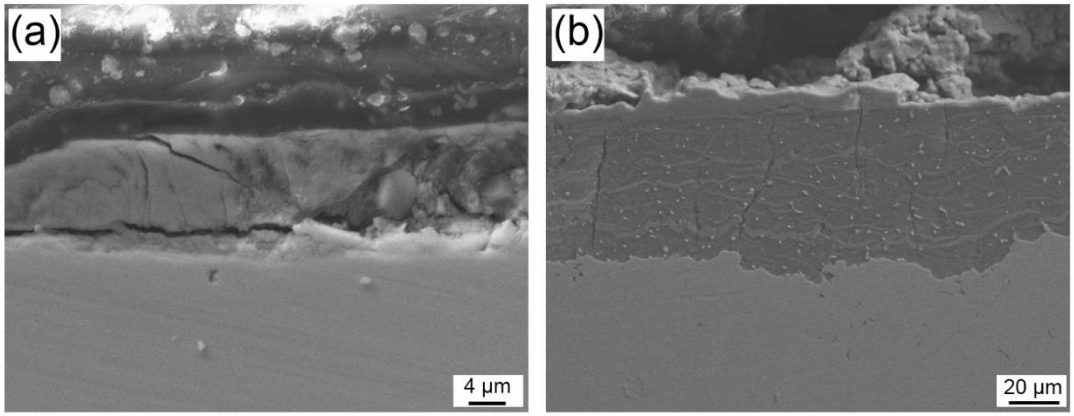

Fig. 3S: Cross section SEM images after 4 months immersion in Hank's solution of (a) Fe10Mn6SiPd and (b) Fe30Mn6SiPd alloys.

Fe-10Mn6Si1Pd after 1 month in Hank's solution

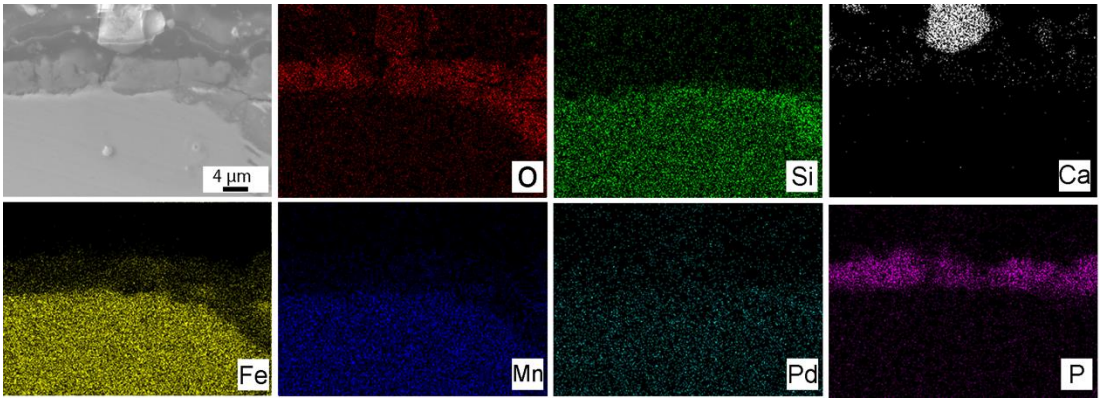

Fe-10Mn6Si1Pd after 4 months in Hank's solution

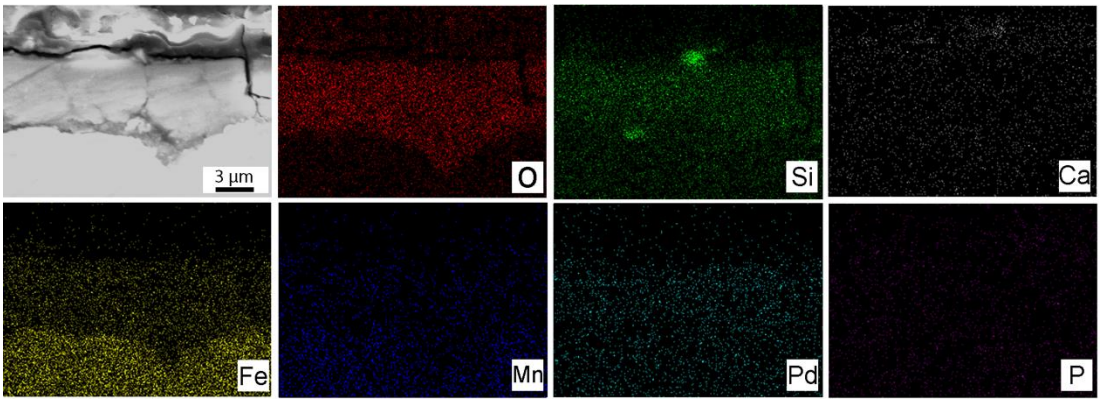

Fe-30Mn6Si1Pd after 1 month in Hank's solution

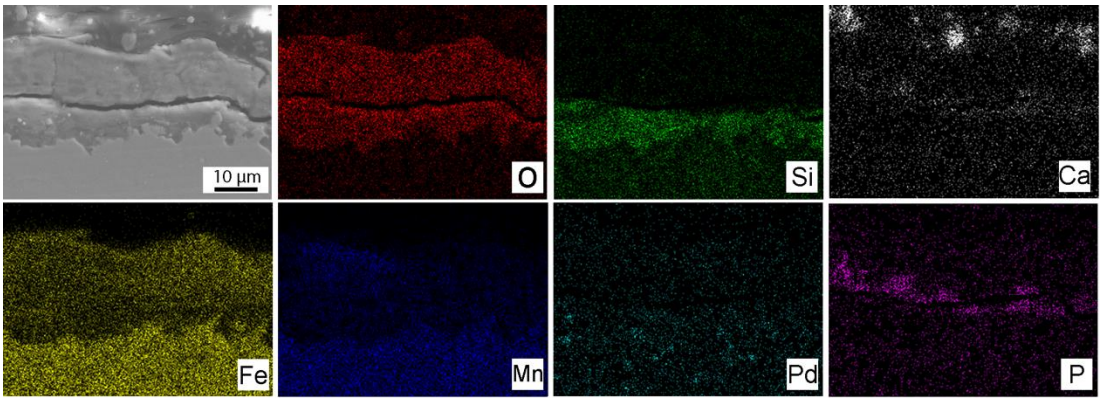

Fig. 4S: Cross section SEM images of Fe-10Mn6Si1Pd (after immersion in Hank's solution for 1 and 4 months) and Fe-30Mn6Si1Pd alloy (after immersion in Hank's solution for 1 month) together with the element distributions of O, Si, Fe, Ca, P, Mn and Pd.

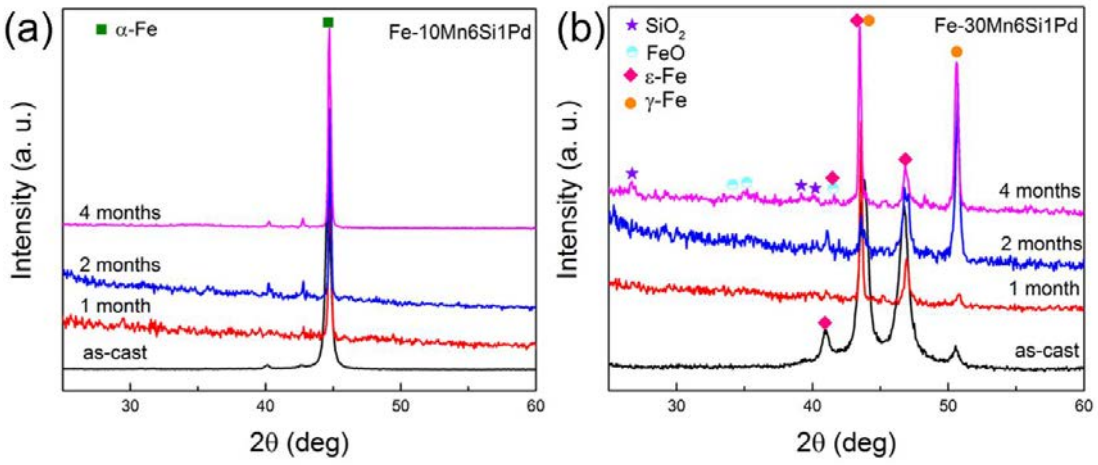

Fig. 5S: XRD analyses of the two quaternary alloys in the as-cast states and after 1, 2 and 4 months of immersion in Hank's solution.

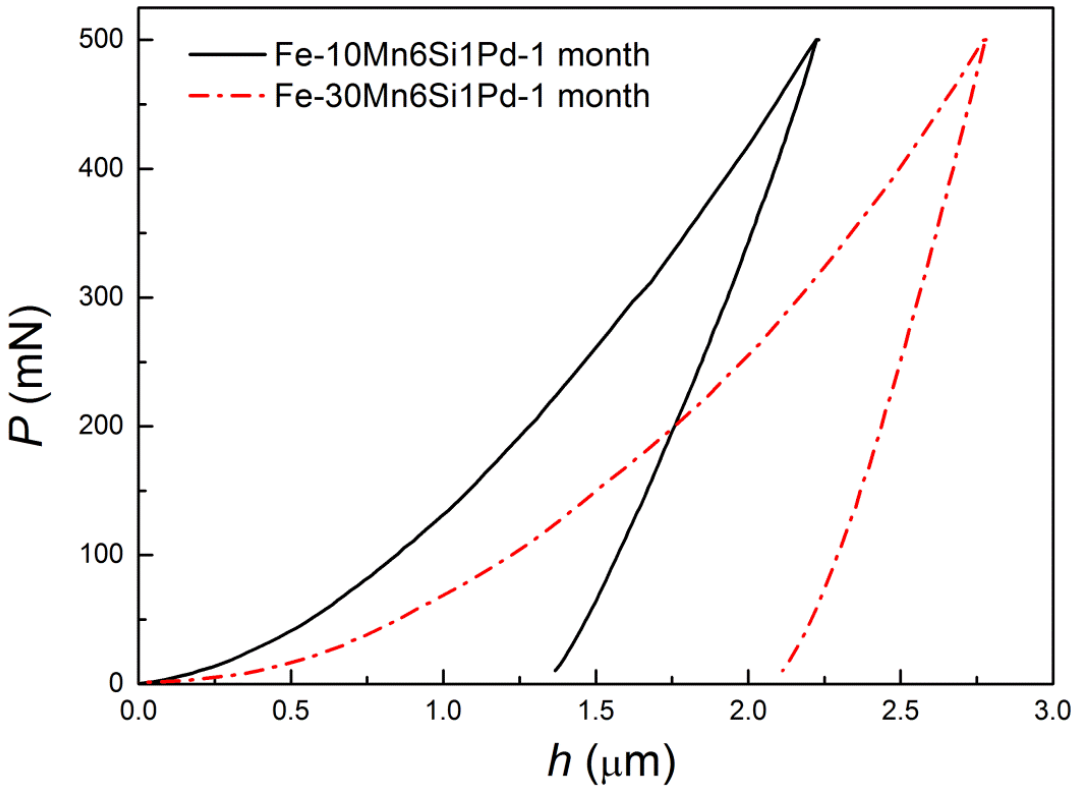

Fig. 6S: Load-unload nanoindentation curves of the Fe-10Mn6SiPd and Fe-30Mn6SiPd alloys measured to a maximum load of 500 mN.

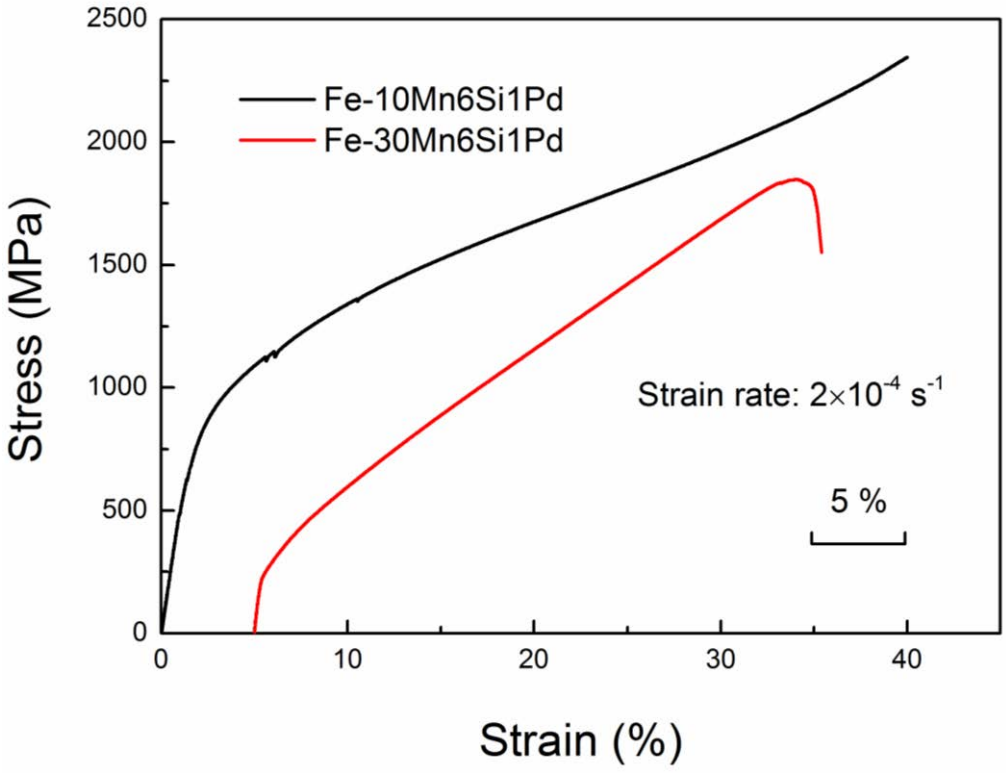

Fig. 7S: Stress-strain compression curves performed on the Fe-10Mn6Si1Pd and Fe-30Mn6Si1Pd alloys, at a strain rate of 2 x 10^{-4} s^{-1}.

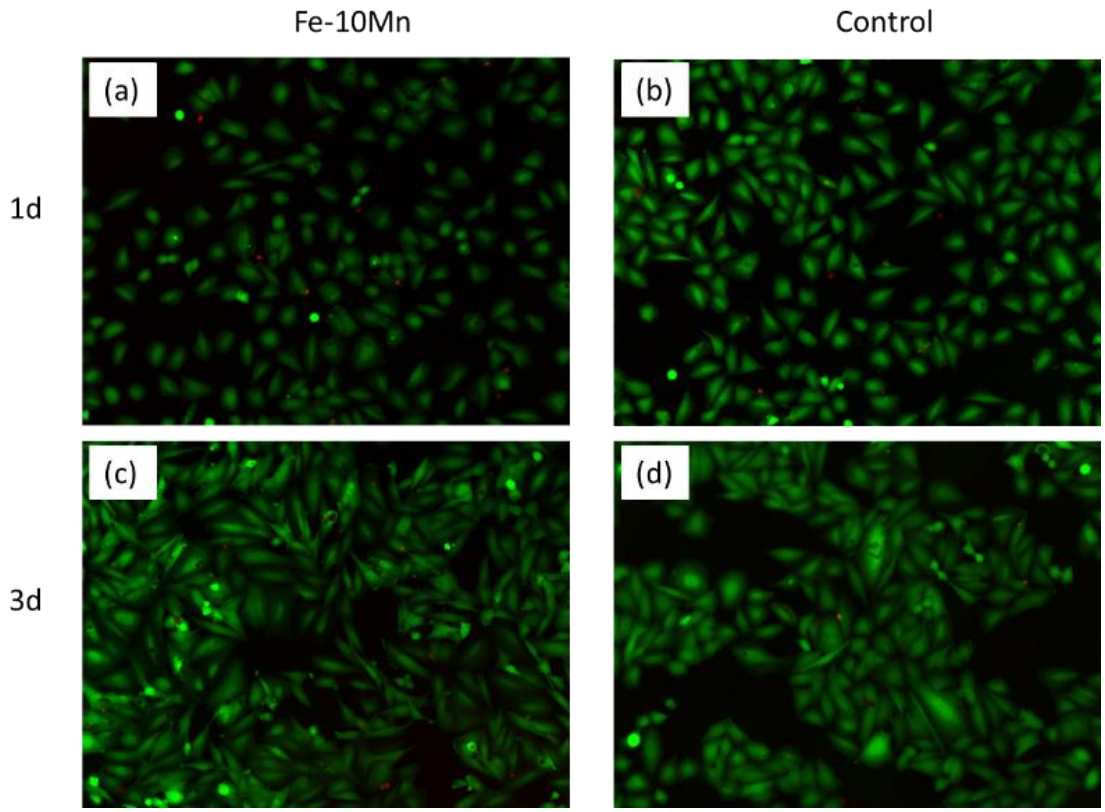

Fig. 8S: Saos-2 cells cultured on the vicinity of Fe-10MnSiPd alloys (indirect study). Cell viability on (a-c) Fe-10MnSiPd and (b-d) control at: (a,b) 1 day, (c,d) 3 days. Live cells stained in green and dead cells stained in red.

3.2 Mechanical properties, corrosion performance and cell viability studies on newly developed porous Fe-Mn-Si-Pd alloys

In this article, porous Fe-30Mn6Si1Pd alloys were prepared by a simple press and sinter process from ball-milled Fe, Mn, Si and Pd powders blended with 10 wt.%, 20 wt.% and 40 wt.% NaCl, as space holding material, rendering different porosity degrees. The obtained open-cell porous Fe-30MnSiPd materials are compared with the bulk fully-compact one synthesized by arc-melting and subsequent copper-mold suction-casting (described in Section 3.1). Based on recent *in-vitro* and *in-vivo* experiments, non-magnetic Fe-30Mn based alloys have established as promising materials for biomedical applications (i.e., in the orthopedics field). However, the mismatch between the mechanical properties of the implant and those of bone, together with their slow degradation into the human body, are some aspects that must be further improved. It is therefore the aim of this work to increase the degradation rate and to lower the Young's modulus of a fully-compact Fe-30Mn6Si1Pd alloy by introducing different degrees of porosity.

The evolution of the microstructure, the mechanical and the magnetic properties during the course of immersion experiments has been investigated. The eventual cytotoxicity of all these alloys has also been assessed in terms of cell viability and cell proliferation.

Our results reveal that by increasing the amount of NaCl from 10 to 40 wt.%, the Young's modulus decreases from 55 GPa to 7 GPa, hence matching the Young's modulus of human bone. While the porous Fe-30Mn6Si1Pd alloys only consist of γ-austenite, their fully-compact counterpart comprises ε-martensite and γ-austenite phases. In all cases, the low magnetic susceptibility response assures good compatibility with nuclear magnetic resonance and magnetic resonance imaging techniques.

The biodegradation performance was evaluated by static immersion and electrochemical corrosion tests in Hank's solution. The order of the corrosion

rate is Fe-30Mn6Si1Pd-40%NaCl > Fe-30Mn6Si1Pd-20%NaCl > Fe-30Mn6Si1Pd-10%NaCl > Fe-30Mn6Si1Pd.

Concerning cytotoxicity, the bulk fully-compact and the alloys produced from 10 and 20 % of NaCl are not cytotoxic. However, the alloy obtained from 40%NaCl becomes cytotoxic. From this work, it can be concluded that the faster and higher corrosion and ion release from exceedingly porous specimens compromise their biocompatibility. Hence, low porosities are recommended.

Mechanical properties, corrosion performance and cell viability studies on newly developed porous Fe-Mn-Si-Pd alloys

Y. P. Feng[1], N. Gaztelumendi [2], J. Fornell[1,*], H. Y. Zhang[1], P. Solsona[1], M. D. Baró[1], S. Suriñach[1], E. Ibáñez[2], L. Barrios[2], E. Pellicer[1,§], C. Nogués[2], J. Sort[1,3]

[1]Departament de Física, Universitat Autònoma de Barcelona, E-08193 Bellaterra, Cerdanyola del Vallès, Spain

[2]Departament de Biologia Cel·lular, Fisiologia i Immunologia, Universitat Autònoma de Barcelona, E-08193 Bellaterra, Cerdanyola del Vallès, Spain

[3] ICREA, Pg. Lluís Companys 23, E-08010 Barcelona, Spain

Corresponding author. E-mail addresses:

*Jordina.Fornell@uab.cat, §Eva.Pellicer@uab.cat

Journal of Alloys and Compounds 724 (2017) 1046–1056

Contents lists available at ScienceDirect

Journal of Alloys and Compounds

journal homepage: http://www.elsevier.com/locate/jalcom

Mechanical properties, corrosion performance and cell viability studies on newly developed porous Fe-Mn-Si-Pd alloys

Y.P. Feng [a], N. Gaztelumendi [b], J. Fornell [a, *], H.Y. Zhang [a], P. Solsona [a], M.D. Baró [a], S. Suriñach [a], E. Ibáñez [b], L. Barrios [b], E. Pellicer [a, **], C. Nogués [b], J. Sort [a, c]

[a] Departament de Física, Universitat Autònoma de Barcelona, E-08193, Bellaterra, Cerdanyola del Vallès, Spain
[b] Departament de Biologia Cellular, Fisiologia i Immunologia, Universitat Autònoma de Barcelona, E-08193, Bellaterra, Cerdanyola del Vallès, Spain
[c] ICREA, Pg. Lluís Companys 23, E-08010, Barcelona, Spain

ARTICLE INFO

Article history:
Received 15 February 2017
Received in revised form
20 June 2017
Accepted 8 July 2017
Available online 12 July 2017

Keywords:
Porous alloys
Open-cell Fe-based foam
Space holder
Mechanical properties
Biomaterials
Cytotoxicity

ABSTRACT

Porous Fe-30Mn6Si1Pd (wt.%) alloys were prepared by a simple press and sinter process from ball-milled Fe, Mn, Si and Pd powders blended with 10 wt%, 20 wt% and 40 wt% NaCl to obtain different degrees of porosity. For comparison purposes, a bulk fully-compact Fe-30Mn6Si1Pd alloy was produced by arc-melting and subsequent copper-mold suction-casting. While the porous Fe-30Mn6Si1Pd alloys only consist of γ-austenite, their fully-compact counterpart comprises ε-martensite and γ-austenite phases. In all cases, the low magnetic susceptibility response assures good compatibility with nuclear magnetic resonance and magnetic resonance imaging techniques. Furthermore, a reduction of the Young's modulus, from 55 to 7 GPa, was attained by introducing porosity. The biodegradation performance was evaluated by static immersion and electrochemical corrosion tests in Hank's solution. The influence of immersion time on composition, microstructure, mechanical and magnetic properties was assessed. While introducing porosity renders alloys with suitable mechanical and magnetic properties, it also has a detrimental effect in terms of cell viability. Hence, the porosity level needs to be controlled in order to obtain alloys with an optimized performance.\

1. Introduction

The development of metallic materials for permanent implant applications such as Ti alloys, 316L stainless steels and Co-Cr alloy has been a subject of intense research in recent years because of their high corrosion resistance, good biocompatibility and excellent mechanical properties [1–3]. However, a secondary surgery for implant removal is often necessary to avoid long-term complications, such as chronic inflammation, possible subsequent thrombosis and systemic toxicity [4,5]. To overcome this drawback, biodegradable metallic implants emerged as a novel class of biomaterials, improving the patient's comfort and reducing the cost of medical treatment [6–12].

Mg-based and Fe-based alloys are the two main types of biodegradable metallic materials considered as potential candidates for temporary medical biodegradable implants, such as stents or bone replacements [6–9]. Mg-based degradable alloys have been, by far, the most extensively explored ones because of their fast biodegradability and Young's modulus closer to that of human bone. However, the degradation rate of Mg-based biomaterials in the human body is typically exceedingly fast and this causes a loss of their mechanical integrity before the patient fully recovers. Another issue with Mg-based biomaterials is the considerable amount of hydrogen release, which prolongs the healing process and impedes a good connectivity between osteocytes and the implant. To tackle these issues, in the last few years, more attention is being paid to Fe-based alloys. Typically, Fe-based alloys exhibit good biocompatibility and competitive mechanical properties; however, in most cases, their degradation in the human body is too slow. The most explored approach to increase their degradation rate without compromising the strength is the addition of certain biocompatible elements (i.e., P, Mn, Pd, etc.) [6,10–14]. Furthermore, a careful selection of potential alloying elements is required to avoid non-ferromagnetic properties, which would hinder the utilization of nuclear magnetic resonance (NMR)

* Corresponding author.
** Corresponding author.
E-mail addresses: Jordina.Fornell@uab.cat (J. Fornell), Eva.Pellicer@uab.cat (E. Pellicer).

http://dx.doi.org/10.1016/j.jallcom.2017.07.112
0925-8388/

or magnetic resonance imaging (MRI) techniques, required to monitor the patient's recovery after surgery.

Within this framework, FeMn-based alloys [6,10–18] emerged as new materials for biodegradable implants and stents. FeMn alloys with 20–35 wt% Mn (with γ-austenite and ε-martensite microstructures), show a reduced magnetic susceptibility compared to 316L steel [18]. Furthermore, the addition of Mn within the solubility limit of Fe reduces the standard electrode potential of Fe to make it more susceptible to corrosion [11,14]. Therefore, Fe alloys containing 20–35 wt% Mn have been investigated for their potential use as biodegradable implant and stent applications. On the other hand, silicon can increase the strength of the alloy and it is expected to assist the healing process while not causing deleterious effects in the immunologic system, since silicon is an essential mineral in the human body [17,19]. Fe-Mn-Si alloy has been studied for a long time [14,17] because of its shape memory behavior, which may also be of interest for some applications in the biomedical field (e.g., stents) [17].

In our previous study [14], a bulk, fully-compact, Fe-30Mn6Si1Pd alloy was fabricated by arc-melting and copper-mold suction casting. The alloy demonstrated satisfactory magnetic, corrosion properties and good cell viability and proliferation; however, its Young's modulus was too high (93 GPa) when compared to that of the human bone (3–25 GPa) [20]. Making the material porous is an effective way to lower the Young's modulus, as the Young's modulus (and the yield stress) are both proportional to the relative density of the material [21]. Namely, both hardness and Young's modulus progressively decrease with the increase of porosity. Furthermore, porosity increases the overall available surface area of the material to the corrosive environment, which might enhance the degradation process.

In the present work, porous Fe-30Mn6Si1Pd alloys were prepared by a simple press and sinter process from ball-milled Fe, Mn, Si and Pd powders blended with 10 wt%, 20 wt% and 40 wt% NaCl, as space-holding material, rendering different porosity degrees, once NaCl is removed by thermal treatments (sublimation). The obtained open-cell porous FeMnSiPd materials are compared with the bulk fully-compact one synthesized by arc-melting and subsequent copper-mold suction-casting, paying particular attention to the resulting magnetic, mechanical, corrosion resistance and biocompatibility properties. The evolution of the microstructure, the mechanical and the magnetic properties during the course of immersion experiments has also been investigated. Moreover, the eventual cytotoxicity of all these alloys has been assessed in terms of cell viability and cell proliferation. Experiments were performed by culturing the cells during 14 days in conditioned media derived from bulk and porous alloys.

2. Materials and methods

2.1. Materials

Commercial Fe (97%), Si (99%), Mn (99%) and Pd (99.95%) powders were used as starting materials. First, the powders were mixed and mechanically milled in a planetary mill device (Fritsch Pulverisette 5) to obtain the targeted composition, Fe-30Mn6Si1Pd (nominal wt.%). To avoid Mn sublimation, the raw powders were milled under Ar atmosphere with a ball-to-powder weight ratio of 10:1 at 300 rpm for 15 h to induce mechanical alloying. The XRD patterns of the powders milled for 1, 3 and 15 h are shown in Fig. S1. The particle size of the as-milled powders, calculated from an SEM image using the ImageJ software, was 10.8 ± 1.4 μm (Fig. S2). Then, the powders were further mixed with 10 wt%, 20 wt% or 40 wt% NaCl (which will later act as a source of porosity) and milled at 200 rpm for 2 h, to ensure homogeneity. All the operations prior to milling (weighting of the powder and sealing of the container) were done in a glove box under Ar atmosphere (<0.2 O_2 ppm, <0.1H_2O ppm) to avoid oxidation and any other atmospheric contamination. Subsequently, the prepared powder mixtures were uniaxially pressed under a pressure of 100 MPa to obtain pellets of 9 mm in diameter and 2–3 mm in thickness. The NaCl-containing green compacts were loaded in a vacuum furnace and sintered at 900 °C at $5 \cdot 10^{-5}$ mbar for 4 h at a heating rate of 1 °C/min. Because of the hight vapor pressure of Mn, larger sintering temperatures and dwelling times would result in noticeable Mn loss as pointed out by other authors [22,23]. During this process NaCl sublimated, leaving numerous pores beneath. The resulting samples are denoted as Fe-30Mn6Si1Pd-10%NaCl, Fe-30Mn6Si1Pd-20%NaCl and Fe-30Mn6Si1Pd-40%NaCl throughout the manuscript to indicate the parent amount of NaCl used as porogen. The crystal size of NaCl and the pore size of the resulting samples was measured using the Image J software. Density of the sintered samples and hence, the total porosity was calculated according to the Archimedes' principle.

For comparison purposes, a fully-compact Fe-30Mn6Si1Pd alloy (nominal composition) was also produced by arc-melting and subsequent suction-casting. The experimental details concerning the synthesis of this sample are described elsewhere [14]. Optical images comparing the appearance of the bulk fully-compact Fe-30Mn6Si1Pd and Fe-30Mn6Si1Pd-40%NaCl porous alloys are shown in Fig. 1.

The real composition of the as-prepared samples, measured by energy dispersive X-ray spectroscopy (EDX), is Fe-29.2Mn5.2Si1.3Pd (wt.%) for the fully-compact alloy, and Fe-29.1Mn6.1Si0.7Pd1.6O (wt.%), Fe-29.4Mn5.9Si0.7Pd2.0O (wt.%) and Fe-29.4Mn5.8Si0.5Pd1.3O (wt.%) for the alloys produced with 10, 20 and 40 wt% NaCl, respectively. No appreciable difference in the Mn content is observed when comparing the surface composition with the inner composition, which suggests that Mn does not sublimate significantly for the sintering conditions of our work.

2.2. Immersion tests

Prior to immersion tests, pieces of 9 mm in diameter and thickness of 2.5 mm from the as-sintered porous Fe-30Mn6Si1Pd alloys were immersed in 40 mL of Hank's balanced salt solution at 37 ± 1 °C for 7 days, 14 days, and 30 days. For comparison purposes, pieces of 3 mm in diameter and 1 mm thickness of the as-

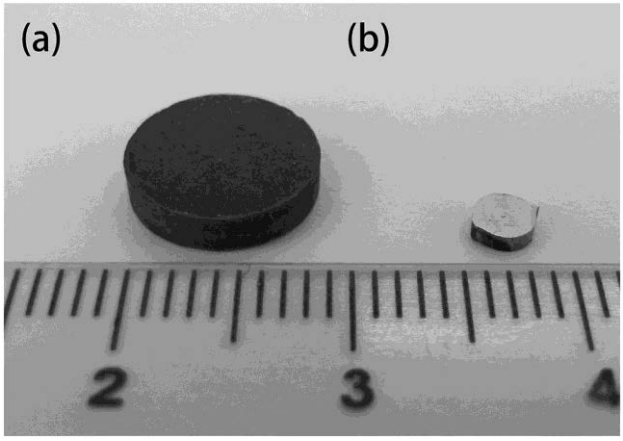

Fig. 1. Image of the (a) porous Fe-30Mn6Si1Pd-40%NaCl alloy obtained by press and sinter process and (b) bulk fully-compact Fe-30Mn6Si1Pd alloy produced by arc melting and subsequent suction mould casting.

cast fully-compact alloy were also immersed in 5 mL of Hank's solution (to maintain the surface-area to solution-volume ratio constant among different samples) for the same periods of time.

The volume of solution was selected to conform with the ASTM-G31-12a norm [24]. After each immersion process, the samples were removed from the Hank's solution, rinsed with alcohol, and dried in air. The microstructure, and the magnetic and mechanical properties were subsequently assessed as a function of immersion time.

2.3. Structural characterization

Scanning electron microscopy (SEM) observations were done on a Zeiss Merlin microscope equipped with an energy dispersive X-ray (EDX) spectroscopy detector for compositional analyses. X-ray diffraction (XRD) was carried out on a Philips X'Pert diffractometer using Cu K_α radiation. The measurements were performed in the angular range $2\theta = 30–100^\circ$ with a step size of 0.026°.

2.4. Characterization of mechanical and magnetic properties

Nanoindentation measurements were carried out on the as-cast and post-immersion samples using a UMIS nanoindenter from Fischer-Cripps Laboratories, with a Berkovich pyramidal-shaped diamond indenter. The maximum applied load was 500 mN. The results were averaged over more than 20 indents for each sample to obtain statistically reliable data. The Berkovich hardness (H) and reduced Young's moduli (E_r) were evaluated from the load–displacement curves, at the beginning of the unloading segments, using the method of Oliver and Pharr [25]. Hysteresis loops were recorded at room temperature using a vibrating sample magnetometer (VSM) from MicroSense, with a maximum applied magnetic field of 20 kOe.

2.5. Electrochemical potentiodynamic polarization measurements

The corrosion behavior of the as-cast and as-sintered alloys was evaluated by potentiodynamic polarization tests in a single compartment, double-walled cell with a typical three-electrode configuration (connected to an Autolab PGSTAT302N potentiostat/galvanostat) at 37 ± 1 °C in Hank's solution. A double junction Ag/AgCl with 3 M KCl inner solution and 1 M NaCl outer solution was used as reference electrode, while a Pt spiral was used as counter electrode, respectively. Prior to the measurements, the specimens were immersed in the electrolyte for 1 h to determine the open circuit potential (OCP). Three samples of each composition were measured to ensure good repeatability. The upper and lower potential limits of the linear sweep voltammetry were set at −1000 mV and +1000 mV. The scan rate was 0.5 mV/s. I_{corr} and E_{corr} were calculated by the classical Tafel analysis which is performed by extrapolating the linear portions of a logarithmic current versus potential plot back to their intersection. The value of either the anodic or the cathodic current at the intersection is I_{corr}.

2.6. Cytotoxicity assays

The human osteosarcoma cell line Saos-2 was used to assess the cytotoxicity of both fully-compact and porous alloys. The Saos-2 cell line was routinely maintained in T25 culture flasks, using DMEM high glucose medium supplemented with 10% Fetal Bovine Serum (FBS) (both from Gibco). To perform the cytotoxicity experiments, 1.5×10^5 cells were seeded into 6-well plates and, once attached to the plate surface, cells were incubated with conditioned medium during 14 days.

To obtain the conditioned medium, alloys were sterilized with dry heat during 3 h at 150 °C and at least 3 disks from each alloy were individually incubated with 4 mL of DMEM +10% FBS in 6-well plates at 37 °C and 5% of CO_2. After 24 h, the conditioned medium, enriched with ions and particles released by the alloys, was pooled, filtered (0.2 μm of diameter from Fisher Scientific) and kept at 4 °C until its use in cell cultures. Fresh medium was added to the same alloy disks and the collection of conditioned medium was repeated using the same procedure at days 3, 7, 10 and 14 from the start of the incubation.

The Live/Dead viability/cytotoxicity kit (Molecular Probes) was used following the manufacturer's instructions for a qualitative analysis of cell viability at 1 and 14 days of culture in conditioned media. This kit allows for the simultaneous detection of living (green fluorescence) and dead (red fluorescence) cells. Images were captured using an Olympus IX71 inverted fluorescence microscope.

The Alamar blue assay (Invitrogen) was used for a quantitative analysis of cell viability and proliferation. Resazurin, the active compound of Alamar Blue, is only reduced to resorufin (a fluorescent product) by viable cells. To perform these experiments, cells were incubated with each conditioned medium as illustrated in Fig. 2. After the corresponding incubation time, the medium was replaced by fresh medium containing 10% of Alamar blue and the cells were incubated for 2 h at 37 °C protected from light. Then, the medium was collected and the fluorescence intensity was measured with a Cary Eclipse Fluorescence Spectrophotometer.

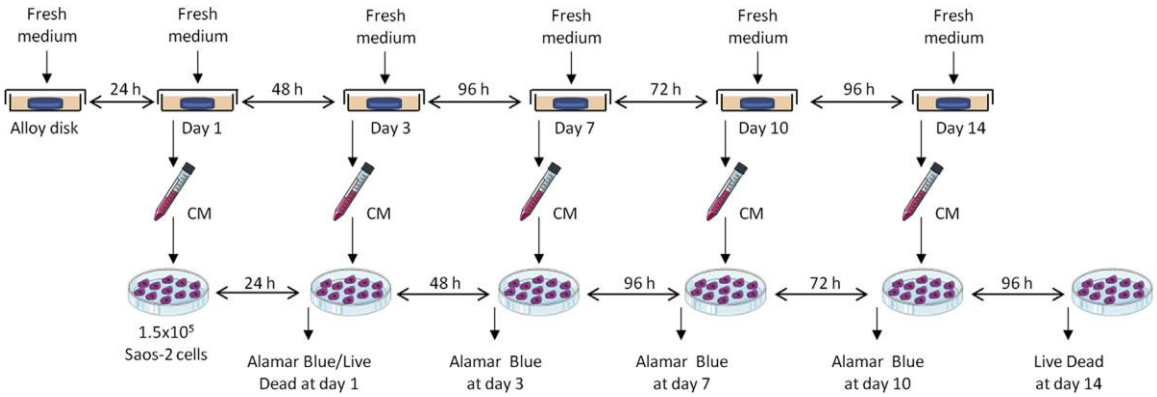

Fig. 2. Diagram representing how the conditioned media is obtained and the procedure followed for the Alamar Blue (at days 1, 3, 7 and 10) and the Live/Dead (at days 1 and 14) assays. At day 1, Alamar blue and Live/Dead assays were independently performed. CM: conditioned medium. (For interpretation of the references to colour in this figure legend, the reader is referred to the web version of this article.)

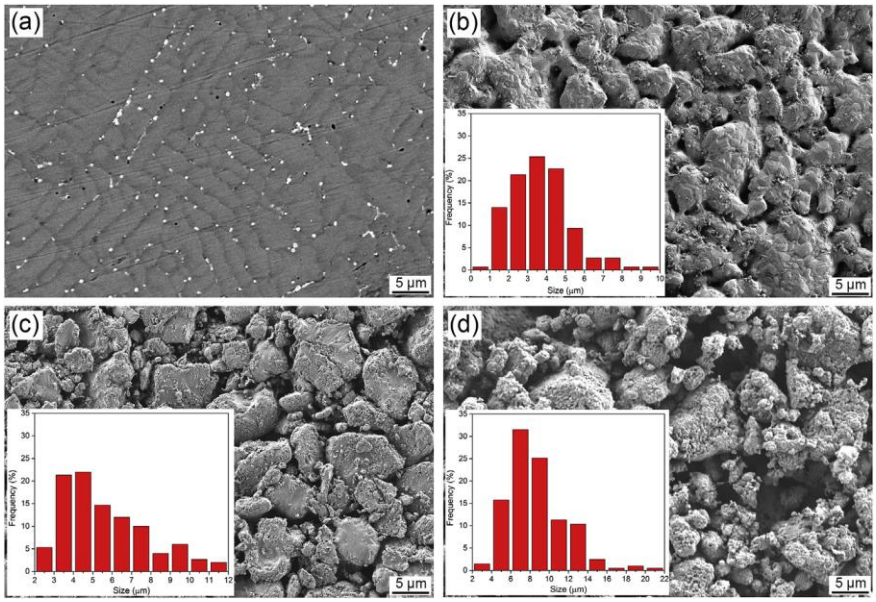

Fig. 3. SEM images of (a) as-cast fully-compact Fe-30Mn6Si1Pd, (b) Fe-30Mn6Si1Pd-10%NaCl, (c) Fe-30Mn6Si1Pd-20%NaCl and (d) Fe-30Mn6Si1Pd-40%NaCl porous as-prepared alloys. The insets show the pore size distribution for the sintered alloys.

Results are the average of three independent experiments performed for each alloy and condition. Control cultures with fresh medium were also performed in triplicate. The ANOVA test for multiple comparisons was used to assess statistical differences in the mean values of living cells cultured in conditioned medium from the different materials at each time point. Data was normalized with control cultures, and significance was considered for $p < 0.05$.

3. Results and discussion

3.1. Microstructure and compositional analyses

3.1.1. Morphology, chemical composition and crystallographic phase composition of the as-prepared alloys

Fig. 3 shows top-view SEM micrographs of as-cast fully-compact Fe-30Mn6Si1Pd (panel a), Fe-30Mn6Si1Pd-10%NaCl (panel b), Fe-30Mn6Si1Pd-20%NaCl (panel c) and Fe-30Mn6Si1Pd-40%NaCl (panel d) as-prepared alloys. In the fully-compact Fe-30Mn6Si1Pd alloy, the typical dendritic morphology, together with Pd-rich precipitates [14], can be observed. Such dendritic morphology is not detected in the porous counterparts. In that case, depending on the amount of NaCl, different degrees of porosity, as well as differences in the pore size, are observed. The porosity mainly originates from the decomposition of the porogen NaCl crystals; therefore, larger amounts of NaCl give rise to more porous specimens [26]. Pore size also tends to increase with increasing the amount of NaCl as a result of the larger chances of coalescence between NaCl crystals. Zhang et al. [27] also reported that pore sizes larger than the crystal size could be obtained when employing NH_4HCO_3 as a porogen, when the spacer amount was up to a certain value (20 vol%). The pore size histograms of the as-prepared porous alloys are shown in the insets of Fig. 3. The average pore size values in the alloys with 10, 20 and 40 wt% of NaCl are 3.7 ± 1.5 μm, 5.7 ± 2.3 μm and 8.6 ± 3.0 μm, while the size of the NaCl powders after ball milling is 4.4 ± 1.9 μm. Hence coalescence and interconnection between neighboring NaCl particles indeed took place for large NaCl contents. It is also worthy to mention that the alloy particles exhibit intrinsic nanometer-size porosity, independently of the amount of NaCl, as a result of the compaction and sintering process.

The porosity and the density of the sintered alloys are listed in Table 1. As expected, the addition of NaCl significantly increases the porosity of the compacts (i.e., the alloys produced with 10 wt% of NaCl show a 25.9% porosity while those produced with 40 wt% of NaCl resulted in 62.3% of porosity).

Fig. 4 illustrates the XRD patterns of the as-cast fully-compact and as-prepared porous Fe-30Mn6Si1Pd alloys. The as-cast bulk Fe-30Mn6Si1Pd is composed of ε-martensite ($P6_3/mmc$, a = 2.55 Å, c = 4.14 Å) and retained γ-austenite (Fm3m, a = 3.60 Å) phases. Conversely, only γ-austenite (together with minor reflections belonging to oxide formation) can be observed in the XRD patterns of the porous Fe-30Mn6Si1Pd alloys. The structural differences observed among the bulk and porous alloys can be attributed to the technique used to fabricate the alloys rather than to changes in composition. In the fully-compact alloys, the higher cooling rate achieved during suction casting into a refrigerated Cu mould promotes the austenite-to-martensite phase transformation. Nonetheless, the cooling rate was not high enough and retained austenite was kept mixed with the martensite phase. Conversely, the sintered powders were cooled from 900 °C to room temperature inside a furnace, hence with a much slower cooling, favoring the complete formation of austenite phase.

Table 1
% of porosity and density measured using the Archimedes' principle for the alloys produced with 10, 20 and 40 wt% of NaCl.

Wt.% NaCl	Porosity (%)	Density (g/cm3)
10	25.9	5.3
20	41.3	4.2
40	62.3	2.7

3.1.2. Morphology, chemical composition and crystallographic phase composition analyses as a function of immersion time

Fig. 5 compares the SEM images of the fully-compact and porous

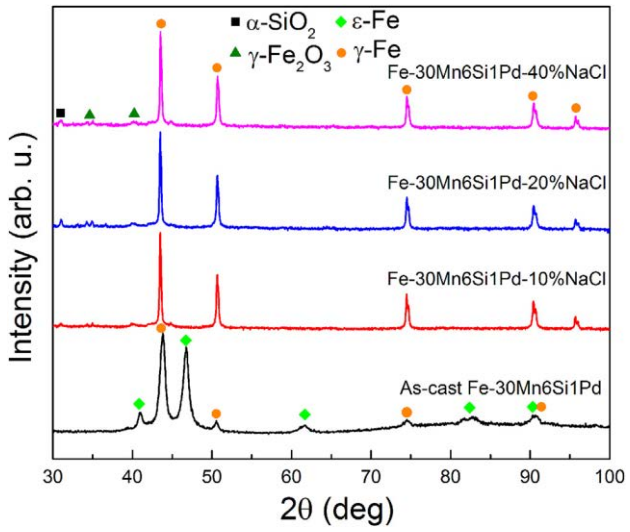

Fig. 4. XRD patterns of as-cast Fe-30Mn6Si1Pd, Fe-30Mn6Si1Pd-10%NaCl, Fe-30Mn6Si1Pd-20%NaCl and Fe-30Mn6Si1Pd-40%NaCl as-prepared alloys.

alloys after immersion in Hank's solution for 30 days. While in the bulk Fe-30Mn6Si1Pd alloy (panel a) a compact and smooth oxide layer on the outermost surface was previously identified [14], the corrosion products for the porous Fe-30Mn6Si1Pd alloys (panels b, c and d) were coating the Fe-based particles in a non-continuous manner. For the Fe-30Mn6Si1Pd-10%NaCl, the porous structure almost collapsed and considerably smaller voids are observed compared to the as-prepared alloy (i.e., the porous structure is almost lost). Similar morphology can be observed in the Fe-30Mn6Si1Pd-20%NaCl alloy although, in this case, some of the pores are still visible, although being smaller. On the contrary, the porous structure of the Fe-30Mn6Si1Pd-40%NaCl sample clearly remains after 30-days immersion. To shed light on the degradation mechanisms of these alloys, cross section SEM images after 30 days immersion in Hank's solution are presented in Fig. 6 for the as-cast fully-compact and for the porous (20 wt% NaCl) specimens. While for the fully-compact Fe-30Mn6SiPd alloy a compact 3–5 μm thick oxide layer can be observed at the outermost surface, no evidence of such a compact and continuous oxide-hydroxide layer can be observed anywhere for the Fe-30Mn6Si1Pd-20%NaCl alloy. Remarkably, in this case, the corrosion products were attached at the surface of the alloy particles throughout the thickness (i.e., filling the pores), as the Hank's solution can permeate through the open-cell porous structure of the alloy.

A detailed cross section SEM image of the Fe-30Mn6Si1Pd-20% NaCl alloy after immersion in Hank's solution for 30 days, together with the O, Si, Fe, Mn and Pd element distribution mappings, are shown in Fig. 7. The trend is the same for the Fe-30Mn6Si1Pd-10%NaCl and Fe-30Mn6Si1Pd-40%NaCl alloys. The mappings reveal that the pores are filled with corrosion products enriched in Si and O and depleted in Fe and Mn. Si is known to be an element prone to oxidation. In fact, in alkaline solutions, the standard reduction potential (E^o) for the reaction $SiO_3^{2-} + 3H_2O + 4e^- \rightarrow Si + 6OH^-$ is −1.69 V. Meanwhile, the standard potential values for Pd, Fe and Mn are: $E^{o2+}_{Pd/Pd} = 0.95$ V, $E^{o2+}_{Fe/Fe} = -0.44$ V and $E^{o2+}_{Mn/Mn} = -1.18$ V [28]. Therefore, among all

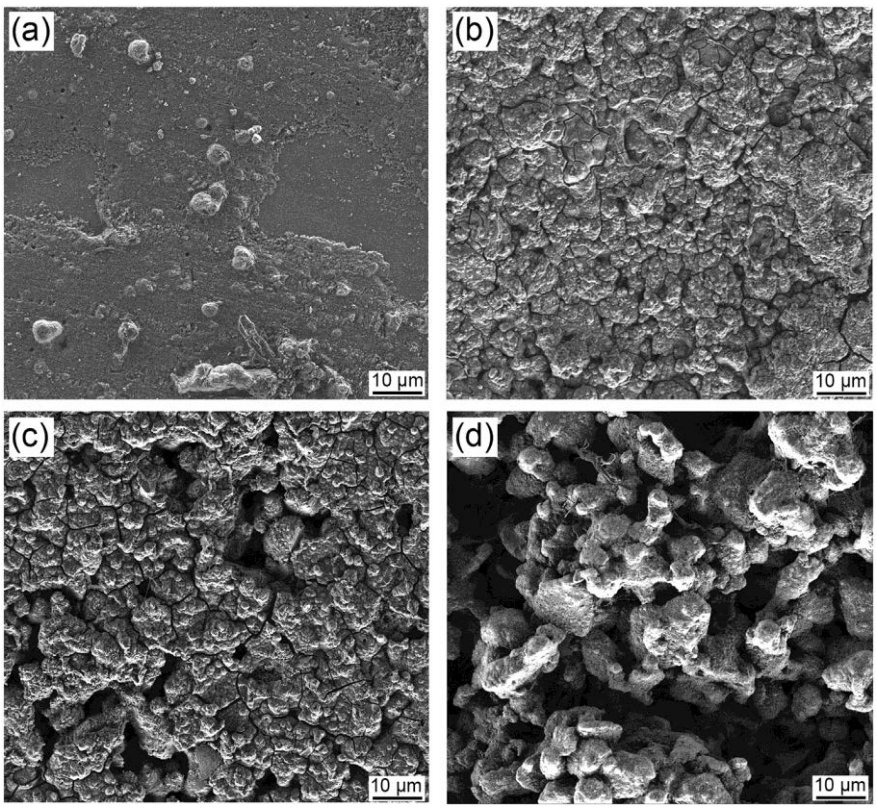

Fig. 5. SEM images of (a) Fe-30Mn6Si1Pd, (b) Fe-30Mn6Si1Pd-10%NaCl, (c) Fe-30Mn6Si1Pd-20%NaCl and (d) Fe-30Mn6Si1Pd-40%NaCl after 30 days of immersion in Hank's solution.

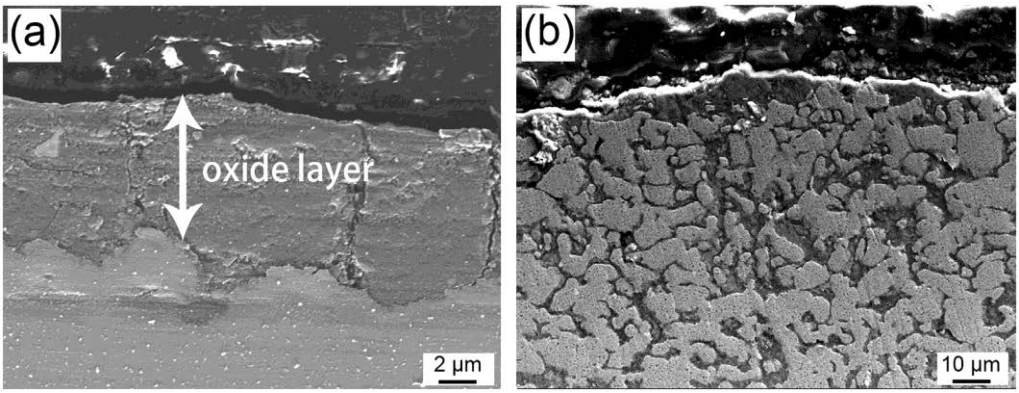

Fig. 6. Cross section SEM images after 30 days immersion in Hank's solution of (a) Fe-30Mn6SiPd and (b) Fe-30Mn6SiPd alloys-20%NaCl.

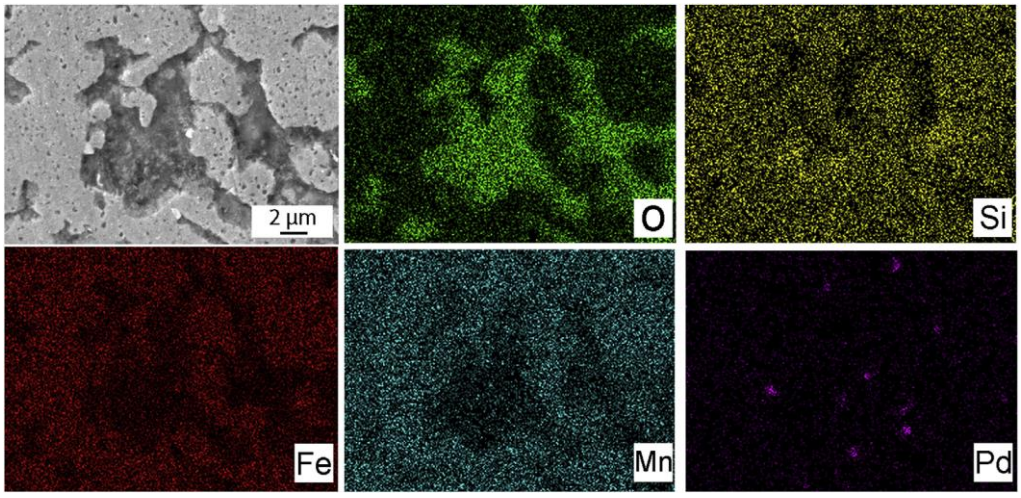

Fig. 7. Cross section SEM images of Fe-30Mn6Si1Pd-20%NaCl after immersion in Hank's solution for 30 days together with the element distributions of O, Si, Fe, Mn and Pd.

these elements, silicon is the one with the more negative standard potential, thus the easiest to oxidize.

After 30 days of immersion in Hank's solution, severe degradation was observed for the porous samples, especially in the Fe-30Mn6Si1Pd-40%NaCl alloy, so the specimens started to disintegrate. The solution became semi-transparent or even opaque with insoluble orange and dark precipitates. These solid precipitates were produced by chemical reaction with the immersion media and they showed relatively low solubility in the aqueous solution, similar to what has been reported for other Fe-based alloys [27].

In order to gain further insight into the corrosion products formed on the surface of the sample during immersion, XRD was carried out on the Fe-30Mn6Si1Pd-40%NaCl sample after immersion for 7 days, 14 and 30 days (Fig. 8). However, the XRD patterns taken at 7 and 14 days do not reveal any additional features compared with the as-prepared sample (Fig. 3). This might be attributed to the thin nature of the oxide layer, in good agreement with the on-top SEM observations. XRD could neither capture the pore filling phenomena. This could be due to the limited penetration of X-rays (only a few microns from the surface) or the occurrence of amorphous oxides. A slight increase in the intensity of the oxide peaks is observed after 1 month of immersion in Hank's solution for this sample.

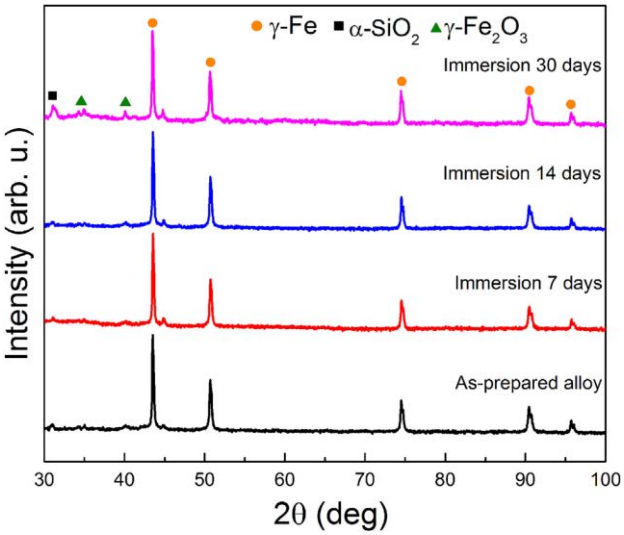

Fig. 8. XRD patterns of Fe-30Mn6Si1Pd-40%NaCl as a function of immersion time in Hank's solution.

3.2. Magnetic properties

The dependence of the magnetization as a function of applied magnetic field for the four as-prepared alloys at room temperature is shown in Fig. 9. Bulk fully-compact Fe-30Mn6Si1Pd alloy shows very low magnetic susceptibility compared to SS316L because of the non-magnetic nature of the γ-austenite (actually the Fe-35Mn alloy has been reported to be antiferromagnetic) [29]. Remarkably, the saturation magnetization of the non-porous Fe-30Mn6Si1Pd (0.4 emu/g) is significantly lower than that of pure Fe (217.2 emu/g) or Fe-10Mn6Si1Pd (160 emu/g) [14]. However, slightly larger saturation magnetization (up to 13.5 emu/g, i.e., still relatively low) is detected for the alloys prepared by powder metallurgy and NaCl sublimation, probably because of the thin layer of iron oxide (Fe_2O_3) formed surrounding the Fe-30Mn6Si1Pd particles. However, in terms of biocompatibility, γ-Fe_2O_3 is a well-accepted magnetic material for biomedical applications, such as targeted delivery, cell labeling, and its excellent biocompatibility has been confirmed [30].

After immersion in Hank's solution for 30 days, the magnetization of the Fe-30Mn6Si1Pd alloys remain almost unaltered (Fig. S3), corroborating that the corrosion products mainly consist of SiO_2 and other non-magnetic oxides and hydroxides.

3.3. Evolution of mechanical properties

The mechanical properties of the as-prepared and immersed alloys were measured by nanoindentation. Nanoindentation is a suitable technique to assess the mechanical properties of bulk materials and films, including porous ones. Indeed, the mechanical properties of dealloyed nanoporous metals and porous oxide films can be reliably estimated by nanoindentation [24]. However, to avoid the influence of the roughness on the extracted mechanical parameters, the samples were indented in the cross-section after having been polished to mirror-like appearance. Another issue to overcome when indenting porous or rough materials is the scattering in the obtained data. This can be particularly troublesome when the size of the indentation imprint does not embrace a representative region of the specimen (i.e., pore size being much larger than the size of the indentation imprint). In this case, the hardness and Young's modulus can locally vary significantly depending on whether the indentation is performed on top of a pore wall or inside a pore. To minimize this problem, we used a maximum load of 500 mN to embrace the maximum representative surface area, as shown in Fig. 10. In addition, several indentations were carried out on different regions of the sample, in order to obtain statistically meaningful data.

The dependences of E_r and H for the Fe-30Mn6Si1Pd-20%NaCl alloy as a function of the immersion time are presented in Fig. 11. The as-prepared Fe-30Mn6Si1Pd-20%NaCl alloy exhibits a Young's modulus of 28 GPa, which is close to that of the human bone (from 3 to 20 GPa). Actually, all the porous Fe-30Mn6Si1Pd samples in the as-produced condition exhibit smaller hardness and Young's modulus than the fully-compact Fe-30Mn6Si1Pd alloy (Fig. S4 and Table 2). Both hardness and Young's modulus progressively reduce with the increase of the porosity level because of the decrease of the relative density of the material [21]. Besides porosity, the fully austenite (mechanically softer phase) structure of the porous alloys probably also contributes to the lower hardness of the porous Fe-30Mn6Si1Pd alloys when compared to the fully-compact one, which also contains martensite (mechanically harder phase).

The mechanical properties of the porous compacts can also be discussed in terms of the classical Gibson-Ashby model, where the porosity of the sintered compacts as well as the pore shape play a role on the resulting mechanical properties. According to the Gibson-Ashby model, the Young's modulus of the porous alloys can be calculated as follows [7,31,32]:

$$E_{porous} = C \cdot E_{bulk} \cdot \left(\frac{\varphi_{porous}}{\varphi_{bulk}}\right)^2 \quad (1)$$

where E_{bulk} is the Young's modulus of the bulk, nonporous alloy (i.e., 93 GPa) [14], C is a geometry constant close to 1 and φ_{porous} is the density of the porous alloy calculated using the Archimedes' principle (Table 1). Good agreement is observed between the Young's modulus measured by nanoindentation and the Young's modulus obtained using Eq. (1). (Table 2).

From Fig. 11, both hardness and Young's modulus increase for immersion times up to 14 days, and then slightly decrease for long-term immersion in Hank's solution. A similar trend was observed

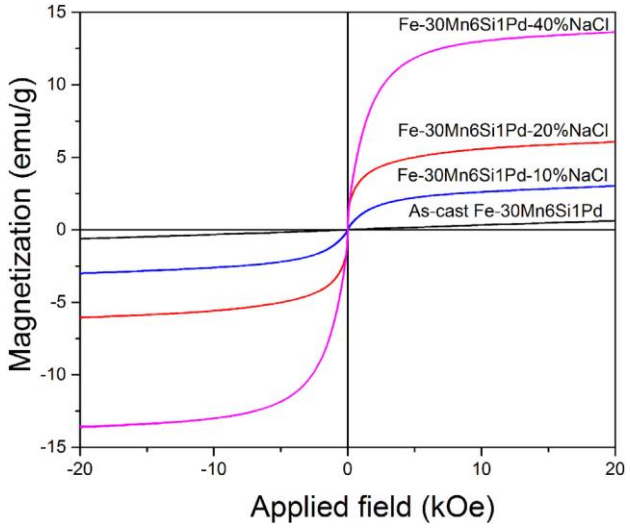

Fig. 9. Dependence of the magnetization as a function of applied magnetic field for as-cast Fe-30Mn6Si1Pd fully-compact alloy, Fe-30Mn6Si1Pd-10%NaCl, Fe-30Mn6Si1Pd-20%NaCl and Fe-30Mn6Si1Pd-40%NaCl porous as-prepared alloys.

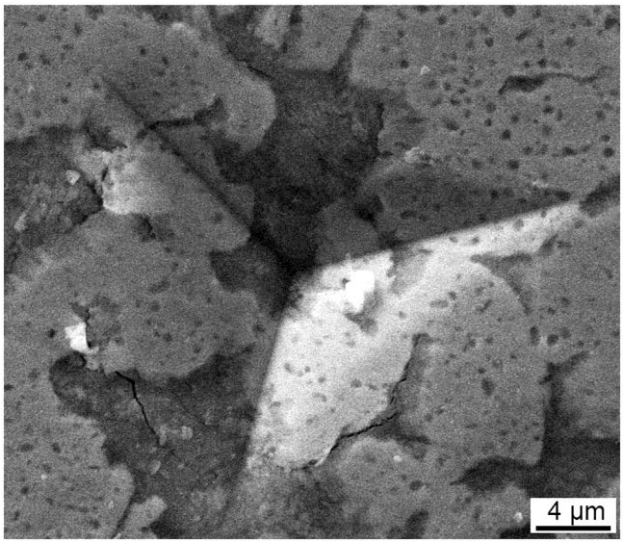

Fig. 10. SEM image of an indent obtained after applying a maximum force of 500 mN in the Fe-30Mn6Si1Pd-20%NaCl after 7 days of immersion in Hank's solution.

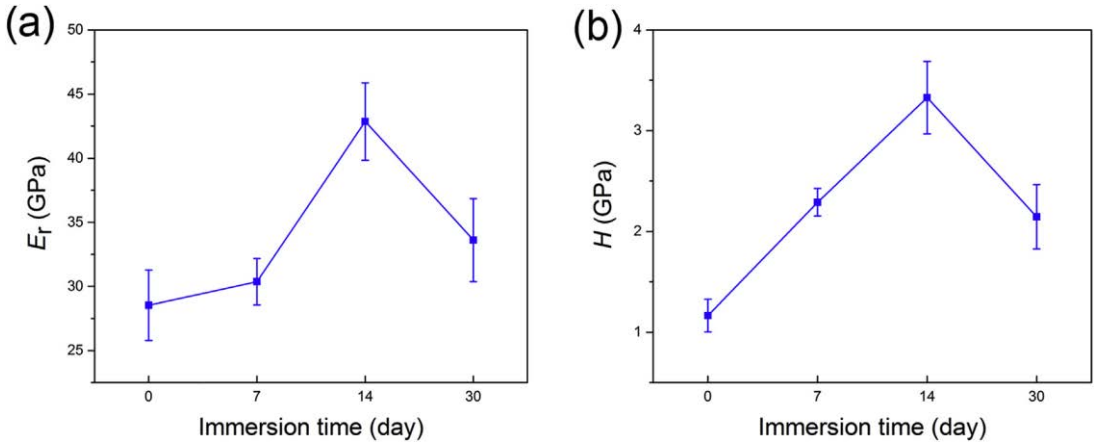

Fig. 11. Dependence of the reduced Young's modulus (E_r) and hardness (H) for Fe-30Mn6Si1Pd-20%NaCl as a function of immersion time.

Table 2
Young's modulus calculated from nanoindentation curves at a maximum applied load of 500 mN and Young's modulus calculated using the Gibson-Ashby model for the alloys produced with 10,20 and 40 wt% of NaCl.

Wt.% NaCl	$E_{nanoindentation}$ (GPa)	$E_{Eq.1}$
10	51.3 ± 2.5	49.3
20	28.5 ± 2.7	32
40	10.2 ± 1	13.2

for the alloys with 10 and 40 wt% of porosity. The increase in hardness and Young's modulus can be attributed to the harder and stiffer nature of the corrosion products filling the holes. However, with prolonged immersion times, these filling oxide materials as well as the alloys themselves, start to lose their integrity, resulting in relatively low Young's modulus. Remarkably, E_r of all the porous alloys reaches values close to 20 GPa after long-term immersion, a value which is close to the Young's modulus of human bones (3–27 GPa), hence favoring good biomechanical compatibility between an eventual implant and the neighboring bone tissue [29].

3.4. Corrosion behavior and corrosion mechanism

The potentiodynamic polarization curves for the four alloys in Hank's solution are shown in Fig. 12. The curves for the porous alloys all display a similar profile. The anodic branch shows an abrupt increase of the current density at −0.6 V once passed the corrosion potential (E_{corr}) an afterwards the current stabilizes. Meanwhile, the fully-compact sample does not show any plateau after crossing E_{corr} and almost immediately undergoes oxidation. In any case, both the corrosion current density (J_{corr}) and E_{corr} are significantly different among samples. J_{corr} is commonly used as a criterion to evaluate the kinetics of a corrosion process as the corrosion rate is normally proportional to J_{corr}. According to Table 3, the order of the corrosion rate is Fe-30Mn6Si1Pd-40%NaCl > Fe-30Mn6Si1Pd-20%NaCl > Fe-30Mn6Si1Pd-10%NaCl > Fe-30Mn6Si1Pd. In addition, the corrosion potential (E_{corr}) follows the same trend, indicating that corrosion initiates at a more cathodic potential as porosity increases. Accordingly, the corrosion resistance (R_p) values diminish. These observations are commonly noted in open-cell porous materials where higher degree of porosity results in larger surface areas exposed to the corrosive media (Hank's solution) [27]. Note that the surface of the non-porous alloy was mechanically polished to mirror-like finish for the electrochemical corrosion experiments. However, the porous specimens were not

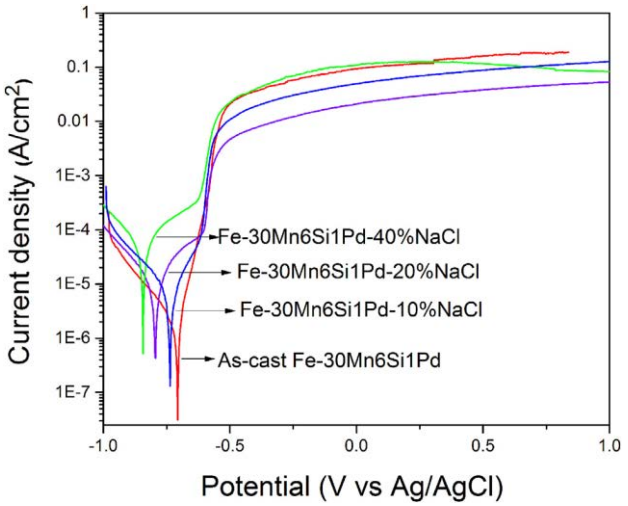

Fig. 12. Potentiodynamic polarization curves for Fe-based alloys in Hank's solution at 37 °C.

Table 3
Electrochemical data calculated from the potentiodynamic polarization corrosion tests.

Wt.% NaCl	Jcorr (A/cm²)	R_p (Ω·cm²)	Ecorr (V vs SCE)
Fe-30Mn6Si1Pd	1.865×10^{-6}	28380	−0.706
Fe-30Mn6Si1Pd-10NaCl	4.466×10^{-6}	21390	−0.737
Fe-30Mn6Si1Pd-20NaCl	2.918×10^{-5}	12570	−0.795
Fe-30Mn6Si1Pd-40NaCl	4.191×10^{-5}	11820	−0.846

polished as this would result in a partial collapse of the pores, hence, significantly altering their surface morphology. Since the chemical composition was highly homogeneous across samples' surface, differences in the corrosion behavior can be directly attributed to the occurrence of porosity. Pores cause a remarkable increase in the surface area of the specimens and, at the same time, act as defects, thereby making the specimens more prone to corrosion. The main degradation mechanism for both, bulk and porous, Fe-30Mn6Si1Pd alloys is based on the electrochemical reaction of the material in contact with the media to produce oxides, hydroxides, hydrogen gas, or other compounds, as it has been reported by many authors [4,15,27]. Our results indicate that the

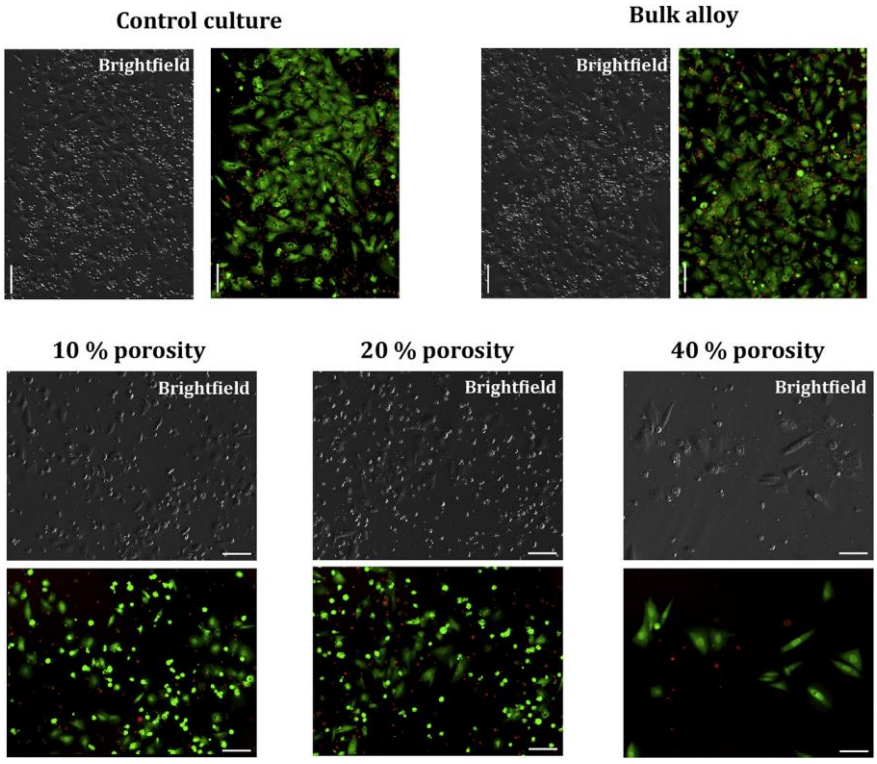

Fig. 13. Living (green) and dead (red) cells after 14 days of culture with conditioned medium. Cell density in bulk alloy and control cultures were higher than in cultures containing conditioned medium from all porous alloys. Only a few cells of the Fe-30Mn6Si1Pd-40%NaCl alloy culture remained attached to the plate surface. Scale bar: 100 μm. (For interpretation of the references to colour in this figure legend, the reader is referred to the web version of this article.)

formation of Si-rich oxides takes place indeed in the porous alloys. In the fully-compact specimen, Ca and P elements could be detected by EDX at the end of the electrochemical polarization tests. The formation of a calcium/phosphorous layer is considered as the last step in the cascade of reactions affecting metallic alloys exposed to simulated body fluids [15]. However, these elements were not detected in its porous counterparts, likely as a result of a faster kinetics of ion release, which would preclude the formation of a stable Ca,P-containing layer.

3.5. Cytotoxicity

Cytotoxicity can promote different cell responses such as necrosis, apoptosis or reduced cell proliferation. The analysis of cell viability only distinguishes between living and dead cells, whereas the analysis of cell proliferation provides additional information on the cell cycle progression, which can be slowed down or even arrested in living cells suffering toxic effects. Thus, for a global measurement of the potential cytotoxicity of bulk and porous alloys, both cell viability and proliferation were assessed at different time-points. The high corrosion and degradation rate of the porous disks surface caused thin layers of material to quickly detach from the alloys surface, preventing cell adhesion during the first 24 h of culture (Fig. S5) and precluding the assessment of cytotoxicity in cells growing directly on the alloys. For this reason, conditioned medium was used to perform the biological experiments. The higher the porosity of the alloys, the larger the loss of integrity of the alloy surface, which is in agreement with the immersion test results.

Qualitative analyses of cell viability showed that on day 1 most of the cells were alive, but the cell density in cultures incubated with conditioned medium was slightly lower than in control cultures, regardless of the type of alloy (Fig. S6). On day 14, cell density decreased in cultures containing conditioned media from all porous alloys compared with those containing conditioned media from the bulk alloy and control cultures (Fig. 13). Quantitative analysis confirmed that there were no significant differences in cell viability between the control and bulk alloy cultures, but the percentage of living cells significantly decreased in all porous alloy cultures (Fig. 14a). In cultures incubated with conditioned medium from the Fe-30Mn6Si1Pd-10%NaCl and Fe-30Mn6Si1Pd-20%NaCl alloys the decrease in cell viability was similar and significantly lower than the decrease observed in 40% porous alloy cultures (Fig. 14a), where only a few living cells remained attached to the plate surface (Fig. 13). Nevertheless, the reduction in cell viability in cultures containing the Fe-30Mn6Si1Pd-10%NaCl and Fe-30Mn6Si1Pd-20% NaCl alloys conditioned medium, although statistically significant when compared to control and bulk alloy cultures, was below 30%, satisfying the ISO 10993-5 standard, which considers a cytotoxic effect when the cell viability is lower than 70%.

Proliferation analyses (Fig. 14b) demonstrated no significant differences between control and bulk alloy cultures, which formed a confluent monolayer on day 7 that was maintained on day 10. Cells cultured in conditioned medium from the Fe-30Mn6Si1Pd-10%NaCl and Fe-30Mn6Si1Pd-20%NaCl alloys also proliferated until day 7, but from then a reduction in the number of cells was observed until day 10. In contrast, cell proliferation in the 40% porous alloy cultures was only observed between days 1 and 3, at very low levels, and from day 3 a progressive reduction in cell number was observed, indicating a high toxicity of this alloy.

In summary, the bulk alloy is not cytotoxic, neither in terms of cell viability nor of proliferation, whereas the Fe-30Mn6Si1Pd-40%

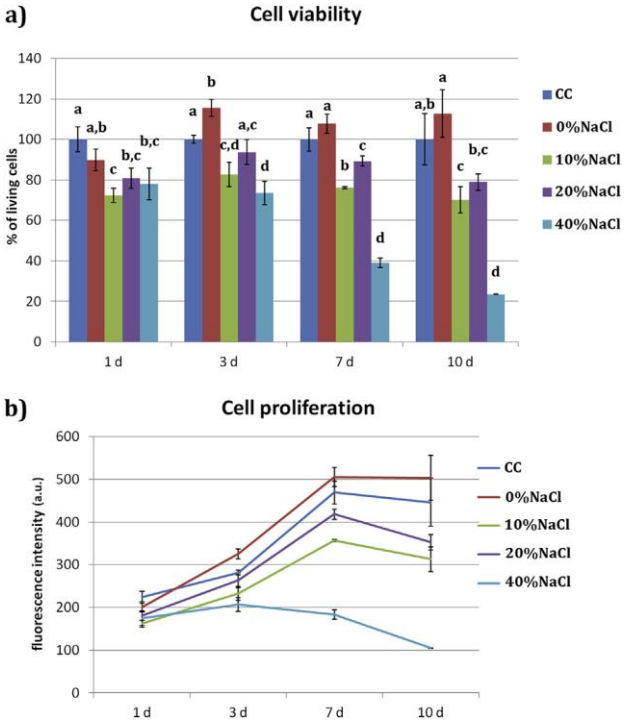

Fig. 14. Cell viability (a) and cell proliferation (b) of Saos-2 cells during 10 days of culture with conditioned media. The percentage of living cells was normalized with control cultures. Arbitrary units (a.u.) were used for cell proliferation. Data are the average of three independent experiments. Significance is represented using an alphabetical superscript system on top of the columns. Letters shared in common among the materials at each time point indicate no significant differences whereas different letters indicate statistically significant differences ($p < 0.05$). CC: control cultures.

NaCl clearly has a cytotoxic effect. This toxicity is probably due to the faster and higher ion release from the porous alloys compared with the bulk one, as shown by the results from the immersion tests and the corrosion characterization.

4. Conclusions

1. While porous Fe-30Mn6Si1Pd alloys are composed by γ-austenite, the bulk fully-compact Fe-30Mn6Si1Pd alloy mainly consists of ε-martensite and γ-austenite Fe-rich phases. Minor contents of Pd-rich precipitates are observed in both bulk and porous materials.
2. The porosity of the Fe-30Mn6Si1Pd alloys increases with increasing the NaCl volume fraction. By increasing the amount of NaCl from 10 to 40 wt%, the Young's modulus decreases from 55 GPa to 7 GPa, hence matching the Young's modulus of human bone.
3. Corrosion resistance is inversely proportional to porosity. E_{corr} shifts to more cathodic values and j_{corr} raises as the porosity of the material increases.
4. Hardness and Young's modulus tend to increase for immersion periods up to 14 days probably because of the formation of mechanically-hard corrosion products (i.e. oxides and hydroxides) filling the pores. However, for longer immersion times, their structural coherence declines, resulting in lower Young's modulus, again not far from that of the human bone.
5. All the investigated alloys are virtually non-magnetic. No significant variations in the overall magnetic properties are observed for immersion times up to 30 days.
6. Bulk alloy is not cytotoxic and does interfere neither with cell viability nor with proliferation.

Fe-30Mn6Si1Pd-10%NaCl and Fe-30Mn6Si1Pd-20%NaCl, according to the ISO 10993-5, cannot be considered cytotoxic. However, the Fe-30Mn6Si1Pd-40%NaCl alloy has a strong cytotoxic effect from day 3 of cell culture. Hence, the faster and higher corrosion and ion release from highly porous specimens compromise their biocompatibility.

Acknowledgments

This work has been partially funded by the 2014-SGR-1015 and the 2014-SGR-524 projects from the Generalitat de Catalunya, and the MAT2014-57960-C3-1-R (co-financed by the *Fondo Europeo de Desarrollo Regional*, FEDER), and the MAT2014-57960-C3-3-R projects from the Spanish *Ministerio de Economía y Competitividad* (MINECO). JF acknowledges the Juan de la Cierva Fellowship from MINECO (IJCI-2015-27030) and EP is grateful to MINECO for the "Ramon y Cajal" contract (RYC-2012-10839).

Appendix A. Supplementary data

Supplementary data related to this article can be found at http://dx.doi.org/10.1016/j.jallcom.2017.07.112.

References

[1] S.V. Muley, A.N. Vidvans, G.P. Chaudhari, S. Udainiya, An assessment of ultra fine grained 316L stainless steel for implant applications, Acta Biomater. 30 (2016) 408–419.
[2] N. Jha, D.P. Mondal, J.D. Majumdar, A. Badkul, A.K. Jha, A.K. Khare, Highly porous open cell Ti-foam using NaCl as temporary space holder through powder metallurgy route, Mater. Des. 47 (2013) 810–819.
[3] E. Zhang, C. Liu, A new antibacterial Co-Cr-Mo-Cu alloy: preparation, biocorrosion, mechanical and antibacterial property, Mater. Sci. Eng. C 69 (2016) 134–143.
[4] Y.F. Zheng, X.N. Gu, F. Witte, Biodegradable metals, Mater. Sci. Eng. R. 77 (2014) 1–34.
[5] Y.W. Song, D.Y. Shan, E.H. Han, Electrodeposition of hydroxyapatite coating on AZ91D magnesium alloy for biomaterial application, Mater. Lett. 62 (2008) 3276–3279.
[6] M. Schinhammer, A.C. Hanzi, J.F. Loffler, P.J. Uggowitzer, Design strategy for biodegradable Fe-based alloys for medical applications, Acta Biomater. 6 (2010) 1705–1713.
[7] E. Pellicer, S. Gonzalez, A. Blanquer, S. Suriñach, M.D. Baró, L. Barrios, et al., On the biodegradability, mechanical behavior, and cytocompatibility of amorphous $Mg_{72}Zn_{23}Ca_5$ and crystalline $Mg_{70}Zn_{23}Ca_5Pd_2$ alloys as temporary implant materials, J. Biomed. Mater. Res. A 101 (2013) 502–517.
[8] P.-C. Wong, P.-H. Tsai, T.-H. Li, C.-K. Cheng, J.S.C. Jang, J.C. Huang, Degradation behavior and mechanical strength of Mg-Zn-Ca bulk metallic glass composites with Ti particles as biodegradable materials, J. Alloy Compd. 699 (2017) 914–920.
[9] Z. Li, M. Chen, W. Li, H. Zheng, C. You, D. Liu, F. Jin, The synergistic effect of trace Sr and Zr on the microstructure and properties of a biodegradable Mg-Zn-Zr-Sr alloy, J. Alloy Compd. 702 (2017) 290–302.
[10] F. Moszner, A.S. Sologubenko, M. Schinhammer, C. Lerchbacher, A.C. Hanzi, H. Leitner, et al., Precipitation hardening of biodegradable Fe–Mn–Pd alloys, Acta Mater. 59 (2011) 981–991.
[11] M. Schinhammer, C.M. Pecnik, F. Rechberger, A.C. Hanzi, J.F. Loffler, P.J. Uggowitzer, Recrystallization behavior, microstructure evolution and mechanical properties of biodegradable Fe–Mn–C(–Pd) TWIP alloys, Acta Mater. 60 (2012) 2746–2756.
[12] T. Kraus, F. Moszner, S. Fischerauer, M. Fiedler, E. Martinelli, J. Eichler, et al., Biodegradable Fe-based alloys for use in osteosynthesis: outcome of an in vivo study after 52 weeks, Acta Biomater. 10 (2014) 3346–3353.
[13] F. Moszner, S.S.A. Gerstl, P.J. Uggowitzer, J.F. Loffler, Atomic-scale characterization of prior austenite grain boundaries in Fe-Mn-based maraging steel using site-specific atom probe tomography, Acta Mater. 73 (2014) 215–226.
[14] Y.P. Feng, A. Blanquer, J. Fornell, H.Y. Zhang, P. Solsona, M.D. Baró, et al., Novel Fe-Mn-Si-Pd alloys: insights into mechanical, magnetic, corrosion resistance and biocompatibility performances, J. Mater. Chem. B 4 (2016) 6402–6412.
[15] H. Hermawan, A. Purnama, D. Dube, J. Couet, D. Mantovani, Fe-Mn alloys for metallic biodegradable stents: degradation and cell viability studies, Acta Biomater. 6 (2010) 1852–1860.
[16] H. Hermawan, H. Alamdari, D. Mantovani, D. Dube, Iron-manganese: new

class of metallic degradable biomaterials prepared by powder metallurgy, Powder Metall. 51 (2008) 38–45.
[17] B. Liu, Y.F. Zheng, L.Q. Ruan, In vitro investigation of Fe30Mn6Si shape memory alloy as potential biodegradable metallic material, Mater. Lett. 65 (2011) 540–543.
[18] H. Hermawan, D. Dube, D. Mantovani, Degradable metallic biomaterials: design and development of Fe-Mn alloys for stents, J. Biomed. Mater. Res. A 93 (2010) 1–11.
[19] Z.G. Xu, M.A. Hodgson, P. Cao, A comparative study of powder metallurgical (PM) and wrought Fe-Mn-Si alloys, Mater. Sci. Eng. A 630 (2015) 116–124.
[20] X.N. Gu, Y.F. Zheng, S.P. Zhong, T.F. Xi, J.Q. Wang, W.H. Wang, Corrosion of, and cellular responses to Mg-Zn-Ca bulk metallic glasses, Biomaterials 31 (2010) 1093–1103.
[21] L.J. Gibson, M.F. Ashby, Cellular Solids: Structure and Properties, second ed., Cambridge University Press, 1999.
[22] Z. Xu, M.A. Hodgson, P. Cao, Weight loss behavior of a vacuum sintered powder metallurgical Fe-Mn-Si alloy, J. Mater. Res. 32 (2017) 644–655.
[23] A. Šalak, M. Selecka, R. Bureš, Manganese in ferrous powder metallurgy, Powder Metall. Prog. 1 (2001) 41–58.
[24] ASTM Standard G31-72, Standard Practice for Laboratory Immersion Corrosion Testing of Metals, ASTM Standards, Philadelphia, PA, USA, 2004.
[25] W.C. Oliver, G.M. Pharr, An improved technique for determining hardness and elastic-modulus using load and displacement sensing indentation experiments, J. Mater. Res. 7 (1992) 1564–1583.
[26] J. Capek, D. Vojtech, A. Oborna, Microstructural and mechanical properties of biodegradable iron foam prepared by powder metallurgy, Mater. Des. 83 (2015) 468–482.
[27] Q. Zhang, P. Cao, Degradable porous Fe-35wt.%Mn produced via powder sintering from NH_4HCO_3 porogen, Mater. Chem. Phys. 163 (2015) 394–401.
[28] W.M. Haynes, Handbook of Chemistry and Physics, 94th ed., CRC Press, 2013.
[29] H. Hermawan, D. Mantovani, Process of prototyping coronary stents from biodegradable Fe-Mn alloys, Acta Biomater. 9 (2013) 8585–8592.
[30] T.R. Pisanic II, J.D. Blackwell, V.I. Shubayev, R.R. Finones, S. Jin, Nanotoxicity of iron oxide nanoparticle internalization in growing neurons, Biomaterials 28 (2007) 2572–2581.
[31] L.J. Gibson, M.F. Ashby, Cellular Solids: Structure and Properties, second ed., Cambridge University Press, Cambridge,, 1997.
[32] D.T. Queheillalt, Y. Katsumura, H.D.G. Wadley, Synthesis of stochastic open cell Ni-based foams, Scr. Mater. 50 (2004) 313–317.

Supporting Information

Mechanical properties, corrosion performance and cell viability studies on newly developed porous Fe-Mn-Si-Pd alloys

Y. P. Feng[1], N. Gaztelumendi [2], J. Fornell[1,*], H. Y. Zhang[1], P. Solsona[1], M. D. Baró[1], S. Suriñach[1], E. Ibáñez[2], L. Barrios[2], E. Pellicer[1,§], C. Nogués[2], J. Sort[1,3]

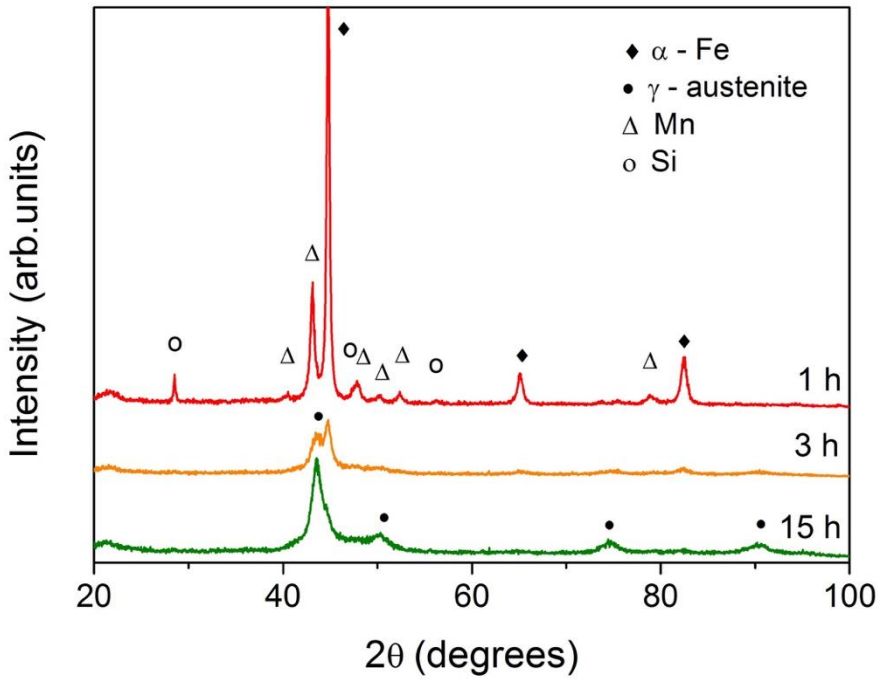

Fig. S1: XRD of the Fe-Mn-Si-Pd powders after 1, 3 and 15 hours of milling.

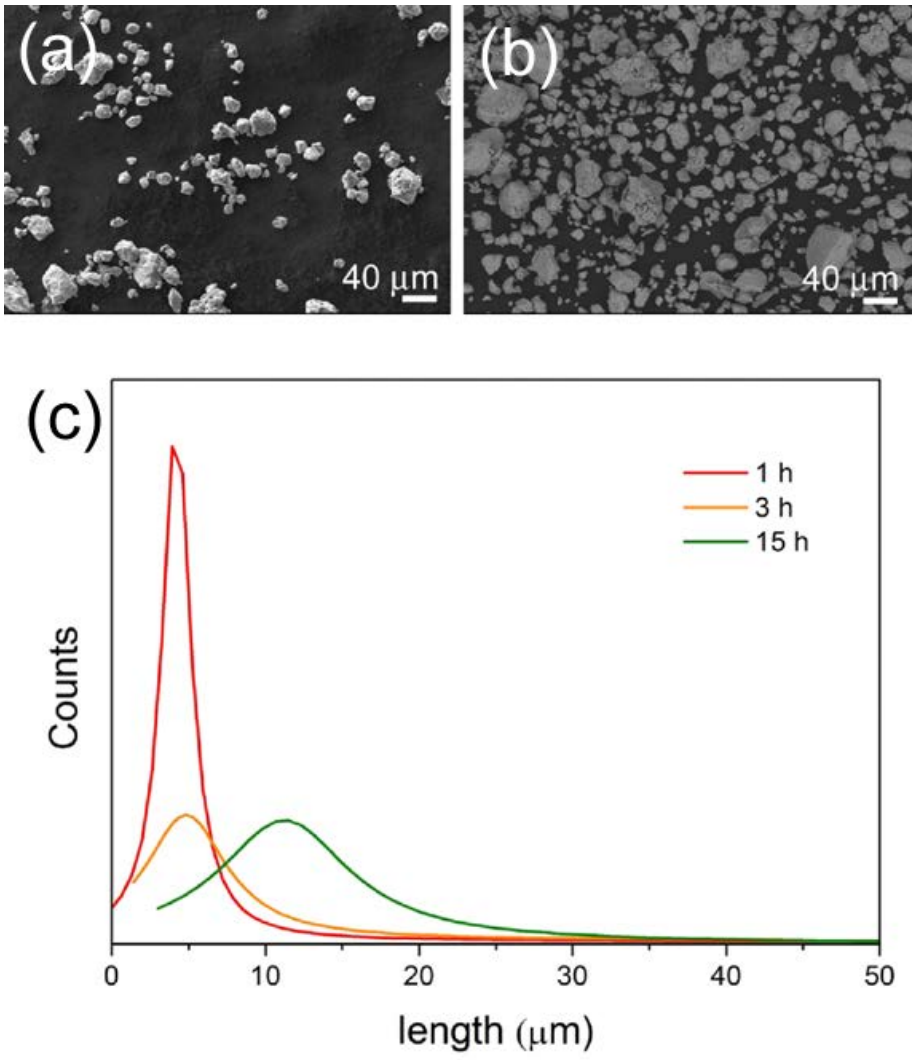

Fig. S2: SEM image of the ball milled powders for a) 1 hour and b) 15 hours. C) Lorentzian fit of the size histogram of the ball milled powders for 1, 3 and 15 hours.

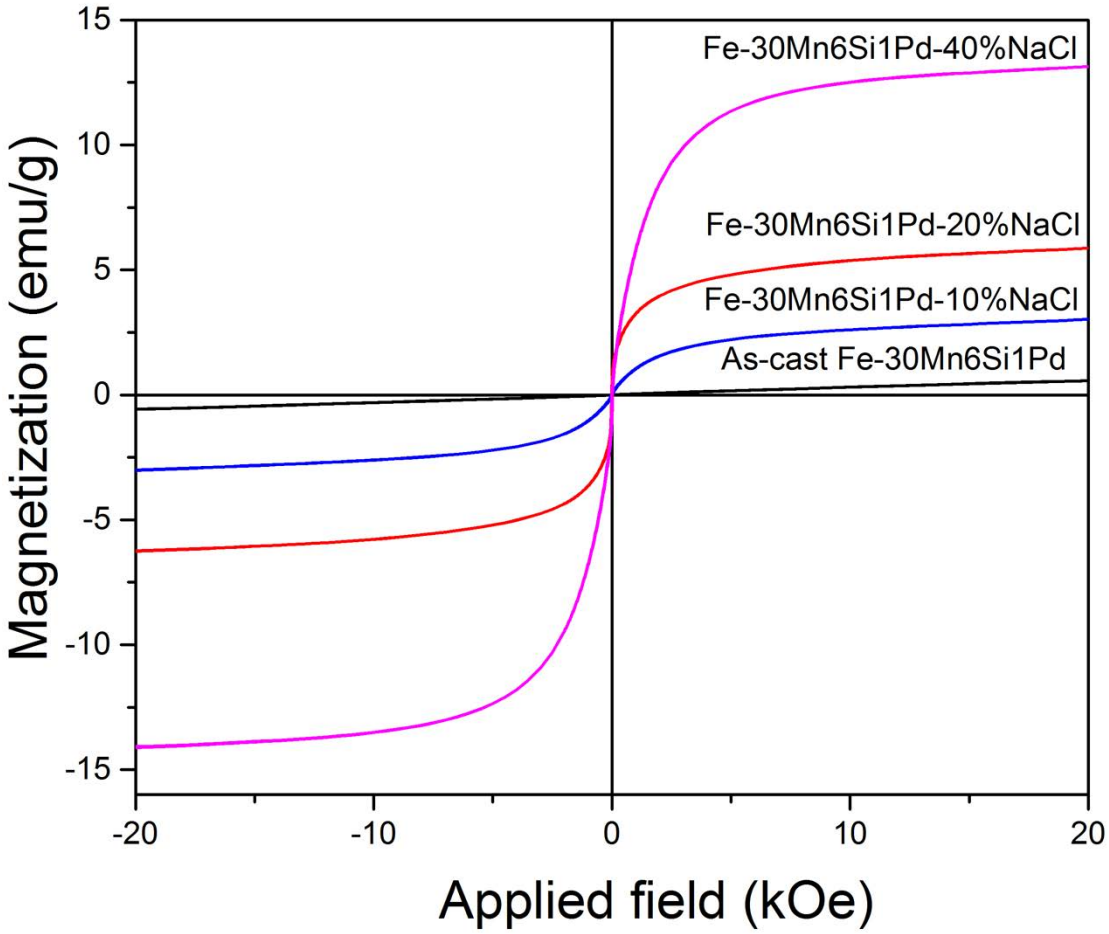

Fig. S3: Dependence of the magnetization as a function of applied magnetic field for fully-compact, as-cast Fe-30Mn6Si1Pd and porous Fe-30Mn6Si1Pd-10%NaCl, Fe-30Mn6Si1Pd-20%NaCl and Fe-30Mn6Si1Pd-40%NaCl alloys after immersion in Hank's solution for 30 days.

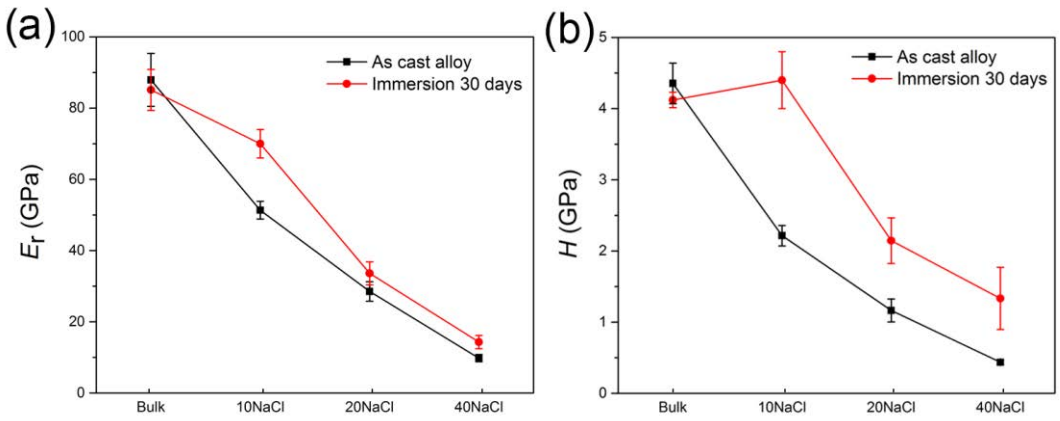

Fig. S4: Reduced Young's modulus (E_r) and hardness (H) for as-prepared Fe-30Mn6Si1Pd, Fe-30Mn6Si1Pd-10%NaCl, Fe-30Mn6Si1Pd-20%NaCl and Fe-30Mn6Si1Pd-40%NaCl before and after immersion in Hank's solution for 30 days.

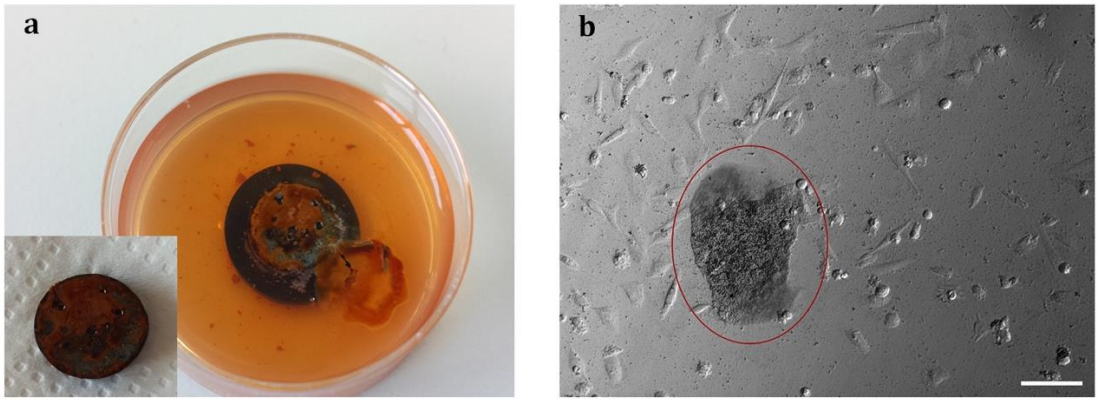

Fig. S5: Alloy surface degradation 24 h after cell seeding: (a) macroscopic view of Fe-30Mn6Si1Pd-40%NaCl alloy degradation (b) debris released from Fe-30Mn6Si1Pd-10%NaCl alloy under an inverted microscope. Scale bar: 100 µm. The inset in (a) shows the formation of an heterogeneous corrosion layer on the alloy surface.

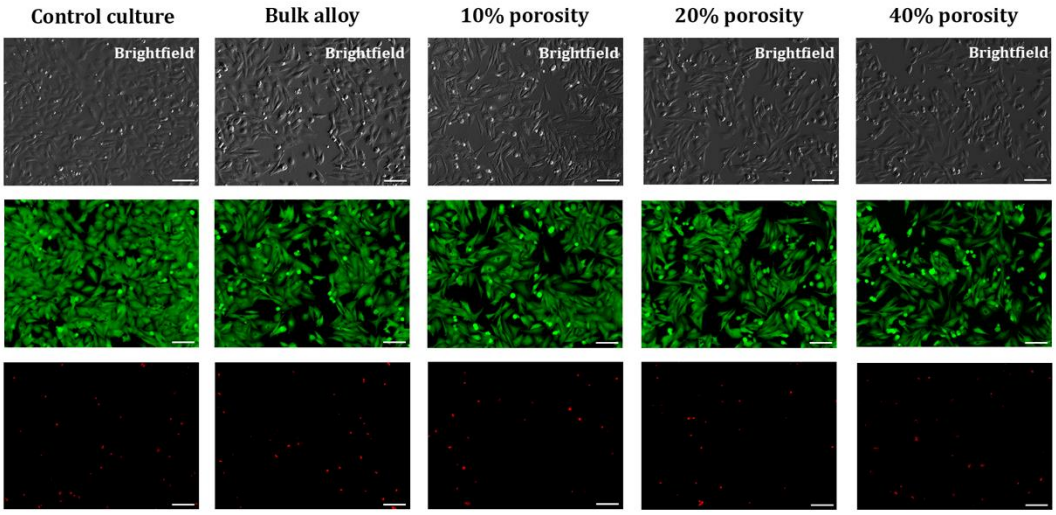

Fig. S6: Living (green) and dead (red) cells after 24 h of cell culture with conditioned medium. A confluent cell monolayer can be seen in control culture whereas cultures incubated with conditioned medium formed subconfluent monolayers. Images were obtained under a flourescence microscope. Scale bar: 100 µm.